Dispersive tsunami waves in the ocean: Model equations and sensitivity to dispersion and Coriolis effects

James T. Kirby [a,*], Fengyan Shi [a], Babak Tehranirad [a], Jeffrey C. Harris [b], Stephan T. Grilli [b]

[a] Center for Applied Coastal Research, University of Delaware, Newark, DE 19716, USA
[b] Department of Ocean Engineering, University of Rhode Island, Narragansett, RI 02882, USA

ABSTRACT

We derive fully nonlinear, weakly dispersive model equations for propagation of surface gravity waves in a shallow, homogeneous ocean of variable depth on the surface of a rotating sphere. A numerical model is developed for the weakly nonlinear version of the model based on a combined finite-volume and finite-difference method with a fourth-order MUSCL-TVD scheme in space and a third-order SSP Runge–Kutta scheme in time. In the context of tsunami generation and propagation over trans-oceanic distances, a scaling analysis reveals that the importance of frequency dispersion increases with a decrease of the source width, while the effect of the Coriolis force increases with an increase of the source width. A sensitivity analysis to dispersive and Coriolis effects is carried out using the numerical model in a series of numerical experiments in an idealized ocean using Gaussian and di-polar sources with different source sizes. A simulation of the Tohoku 2011 tsunami is used to illustrate the effects of dispersive and Coriolis effects at large distances from the source region.

© 2012 Elsevier Ltd. All rights reserved.

1. Introduction

Conventional models used for simulating global-scale tsunamis are traditionally based on the shallow water equations, which neglect frequency dispersion effects on wave propagation. Recent studies, however, reveal that these standard models may not be satisfactory for simulating tsunamis caused by smaller scale or more concentrated non-seismic sources, such as submarine mass failures (SMF) (e.g., Løvholt et al., 2008; Tappin et al., 2008). Moreover, even for very long waves such as found in co-seismic tsunamis, frequency dispersion effects may become significant in the long distance propagation of tsunami fronts. This was evidenced by Kulikov's (2005) wavelet frequency analysis of satellite altimetry data recorded in deep water in the Bay of Bengal during the 2004 Indian Ocean tsunami. Based on these, Kulikov concluded that a dispersive long wave model should be used for this event. In their dispersive numerical simulation of this event, Horillo et al. (2006) concluded that the development in time of the wave front is strongly connected to dispersion effects. Further supporting this conclusion, Glimsdal et al. (2006) and Grue et al. (2008) showed, in their dispersive simulations of this event, that an undular bore could evolve in shallow water, in accordance with other tsunami observations (Shuto, 1985). Finally, using the dispersive Boussinesq model FUNWAVE (Chen et al., 2000; Kennedy et al., 2000) to simulate the same event, Grilli et al. (2007) and Ioualalen et al. (2007) quantified dispersive effects by performing simulations with and without dispersive terms (thus solving nonlinear shallow water equations (NSWE) in the latter case). Differences of up to 20% in surface elevations between Boussinesq and NSWE simulations were found in deeper water.

Regarding effects of sphericity and earth rotation on tsunami propagation, even for the large 2004 event, numerical results showed that a Cartesian implementation of the models (neglecting Coriolis effects) is adequate for regional scale tsunami simulations, provided distances are corrected to account for earth's sphericity (e.g., Grilli et al., 2007; Ioualalen et al., 2007); this is particularly so when the main direction of propagation closely follows a great circle. For global tsunami propagation, however, sphericity and Coriolis effects might play a larger role in simulating tsunami wave arrival at far distant sites. While standard NSWE tsunami simulation models have typically included such effects (e.g., Shuto et al., 1990), dispersive Boussinesq models such as FUNWAVE, which were initially developed for modeling ocean wave transformations from intermediate water depths to the coast, have usually been implemented in Cartesian coordinates without Coriolis effects included. Løvholt et al. (2008) recently developed a Boussinesq model in spherical coordinates, including Coriolis effects. Their simulations quantified the effects of earth's rotation and the importance of Coriolis forces on far-field propagation across the Atlantic Ocean of a potential tsunami originated in La Palma (Canary Islands).

---

* Corresponding author. Tel.: +1 302 831 2438; fax: +1 302 831 1228.
  E-mail address: kirby@udel.edu (J.T. Kirby).

Based on recent work summarized above, it appears that the Boussinesq approximation may be a more accurate tool for performing tsunami simulations relative to more conventional models based on the shallow water theory, since frequency dispersion effects are manifested in almost all cases, either at large distances in larger scale, co-seismic events, or at much shorter distances in smaller scale SMF events. However, the computational demands of such simulations has been a concern. As pointed out by Yoon (2002), Boussinesq models require vast computer resources due to the implicit nature of the solution technique used to deal with dispersion terms. Some simulations may involve a wide range of scales of interest, from propagation out of the generation region, through propagation at ocean basin scale, to runup and inundation at affected shorelines (Grilli et al., 2007). Improvement in model efficiency can be achieved by using nested grids (e.g., Ioualalen et al., 2007; Yamazaki et al., 2011; Son et al., 2011), unstructured or curvilinear grids (Shi et al., 2001) and parallelization of the computational algorithms (Sitanggang and Lynett, 2005; Pophet et al., 2011; Shi et al., 2012a).

In this study, we rigorously derive and validate equations for a dispersive Boussinesq model on the surface of a rotating sphere, including Coriolis effects. The numerical scheme for the weakly nonlinear case is developed following the recent work of Shi et al. (2012a), who applied a TVD Riemann solver to Boussinesq model equations of Chen (2006), extended to incorporate a moving reference level as in Kennedy et al. (2001). The model is implemented using a domain decomposition technique and uses MPI for communication in distributed memory systems. The relative importance of frequency dispersion and Coriolis effects in tsunami propagation is evaluated both theoretically and based on numerical simulations of an idealized case. The basic capability of the model for computing basin-scale tsunami propagation is then demonstrated using the 2011 Tohoku event; more detail of this particular case may be found in Grilli et al. (2012a), where an earlier version of the present model based on depth-averaged velocities is used.

2. Model equations in spherical polar coordinates

We consider the motion of a fluid column with variable still water depth $h'(\phi, \theta)$ on the surface of a sphere of radius r'_0 to the still water level, where coordinates (r', θ, ϕ) denote radial distance from the sphere center, latitude, and longitude, with the local vertical coordinate defined as $z' = r' - r'_0$ (Fig. 1). In this coordinate system, the dimensional Euler equations describing the flow of an incompressible, inviscid fluid are given by (Pedlosky, 1979, Section 6.2),

$$w'_{z'} + \frac{2w'}{r'} + \frac{1}{r'\cos\theta}(v'\cos\theta)_\theta + \frac{1}{r'\cos\theta}u'_\phi = 0 \quad (1)$$

$$\frac{du'}{dt'} + \frac{u'}{r'}(w' - v'\tan\theta) + 2\Omega'(w'\cos\theta - v'\sin\theta) = -\frac{1}{\rho r'\cos\theta}p'_\phi \quad (2)$$

$$\frac{dv'}{dt'} + \frac{1}{r'}(v'w' + (u')^2\tan\theta) + 2\Omega'\sin\theta u' = -\frac{1}{\rho r'}p'_\theta \quad (3)$$

$$\frac{dw'}{dt'} - \frac{(u')^2 + (v')^2}{r'} - 2\Omega'\cos\theta u' = -\frac{1}{\rho}p'_{z'} - g \quad (4)$$

where Ω' is the sphere's angular velocity around the absolute vertical axis, u' and v' are positive velocity components in the horizontal Easterly (ϕ) and Northerly (θ) directions respectively, and w' denotes the local vertical velocity. In the selected coordinate system, the total time derivative operator is defined as,

$$\frac{d()}{dt'} = ()_{t'} + \frac{u'}{r'\cos\theta}()_\phi + \frac{v'}{r'}()_\theta + w'()_{z'} \quad (5)$$
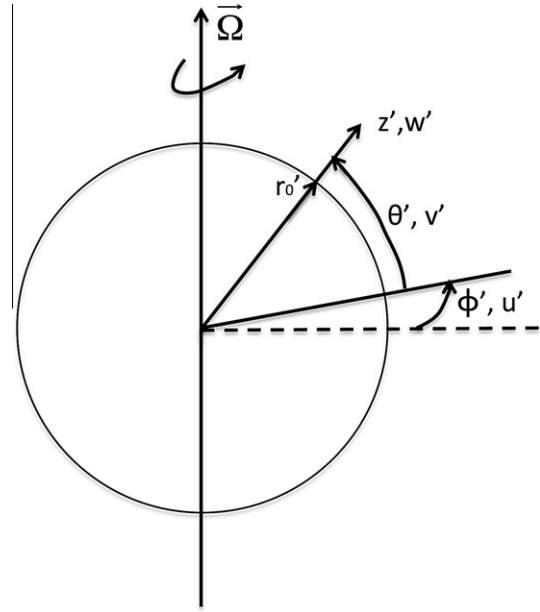

Fig. 1. Coordinate system for model development corresponding to Eqs. (1)–(4).

Boundary conditions consist of a dynamic condition specifying pressure p_s on the free surface,

$$p'_s(\phi, \theta, t') = 0; \quad z' = \eta' \quad (6)$$

together with a kinematic constraints on the velocity field at the surface and bottom boundary. The kinematic surface boundary condition (KSBC) is given by

$$\frac{D\eta'}{Dt'} = w'; \quad z' = \eta' \quad (7)$$

and the (kinematic) bottom boundary condition (BBC) is given by

$$\frac{D(-h')}{Dt'} = w'; \quad z' = -h' \quad (8)$$

where

$$\frac{D()}{Dt'} = ()_{t'} + \frac{u'}{r'\cos\theta}()_\phi + \frac{v'}{r'}()_\theta \quad (9)$$

Note that (8) allows for an imposed motion of the ocean bottom to be specified.

In Boussinesq or shallow water theory, it is typical to replace the local continuity equation (1) with a depth-integrated conservation equation for horizontal volume fluxes. Integrating (1) over depth and employing the kinematic boundary conditions (7) and (8) yields

$$(r')^2|_{\eta'}\eta'_{t'} + (r')^2|_{-h'}h'_{t'} + \frac{1}{\cos\theta}\frac{\partial}{\partial\phi}\left\{\int_{-h'}^{\eta'} u'r'dz'\right\}$$
$$+ \frac{1}{\cos\theta}\frac{\partial}{\partial\theta}\left\{\cos\theta\int_{-h'}^{\eta'} v'r'dz'\right\} = 0 \quad (10)$$

This equation will be simplified below based on scaling arguments.

2.1. Scaling

Based on the standard procedure for shallow water scaling, we introduce the length scales h'_0, a'_0 and λ', denoting a characteristic water depth, wave amplitude (or amplitude of bottom displacement), and horizontal length; with the latter remaining to be

examined. Combining these scales with each other and with r'_0 yields a family of dimensionless parameters: $\epsilon = h'_0/r'_0$ denoting the relative depth or thickness of the ocean layer; $\mu = h'_0/\lambda'$, the usual parameter characterizing frequency dispersion in Boussinesq theory; and $\delta = a'_0/h'_0$, the shallow water nonlinearity parameter. The parameter ϵ takes on values of $O(10^{-3})$ at maximum, and will thus always be taken to indicate vanishingly small effects when it occurs in isolation.

Based on this family of parameters, we scale z-direction quantities by as,

$$(h, z) = \frac{(h', z')}{h'_0}; \quad \eta = \frac{\eta'}{a'_0} \tag{11}$$

We take $u'_0 = \delta c'_0 = \delta\sqrt{gh'_0}$ to denote a scale for horizontal velocities, and let w'_0 denote a scale for vertical velocities, so that,

$$(u, v) = \frac{(u', v')}{u'_0}; \quad w = \frac{w'}{w'_0} \tag{12}$$

Pressure is scaled by the weight of the static reference water column

$$p = \frac{p'}{\rho g h'_0} \tag{13}$$

We introduce a rescaling of the dimensionless latitude and longitude according to

$$(\phi^*, \theta^*) = \frac{r'_0}{\lambda'}(\phi, \theta) = \frac{\mu}{\epsilon}(\phi, \theta) \tag{14}$$

This gives horizontal coordinates which change by $O(1)$ amounts over distances of $O(\lambda')$. Retaining terms to $O(\epsilon)$, the nondimensional form of the continuity equation (1) is then given by

$$\left(\frac{w'_0}{u'_0}\right)[w_z + 2\epsilon w] + \frac{\mu(1 - \epsilon z)}{\cos\theta}[u_{\phi^*} + (v\cos\theta)_{\theta^*}] = O(\epsilon^2) \tag{15}$$

indicating that $w'_0/u'_0 = O(\mu)$, as is usual in a Boussinesq or shallow water model framework. Turning to the depth-integrated mass conservation equation (10), we introduce the total depth,

$$H = h + \delta\eta \tag{16}$$

and obtain

$$\frac{1}{\delta}H_t + \frac{1}{\cos\theta}[(H\overline{u})_{\phi^*} + (H\overline{v}\cos\theta)_{\theta^*}] = O(\epsilon) \tag{17}$$

where

$$(\overline{u}, \overline{v}) = \frac{1}{H}\int_{-h}^{\delta\eta}(u, v)dz \tag{18}$$

are depth-averaged horizontal velocities, and where time t' is scaled according to

$$t = \omega't' = \frac{\sqrt{gh'_0}}{\lambda'}t' \tag{19}$$

In keeping with the notion that waves which are short relative to the basin scale (λ'/r'_0 or $\epsilon/\mu \ll 1$) may have frequencies which are high relative to the earth's rotation rate ($\omega'/\Omega' \gg 1$), we introduce the scaling

$$\Omega = \frac{\mu}{\epsilon}\frac{\Omega'}{\omega'} = O(1) \tag{20}$$

(Comparing to other treatments of this problem, we note that this choice leads to a nondimensional Coriolis term with an explicit scaling that changes its size in the Boussinesq regime in comparison to the shallow water regime, in contrast to the model equations in Løvholt et al. (2008) or Zhou et al. (2011), for example, where the

relative size of local acceleration and Coriolis terms in different scaling limits is not apparent). Turning to the Easterly (ϕ) momentum equation (2), we obtain

$$u_t - \left(\frac{\epsilon}{\mu}\right)fv + \delta\left[\frac{u}{\cos\theta}u_{\phi^*} + vu_{\theta^*} + wu_z - \frac{\epsilon}{\mu}uv\tan\theta\right]$$
$$+ \frac{\delta^{-1}}{\cos\theta}p_{\phi^*}$$
$$= O(\epsilon) \tag{21}$$

where the dimensionless Coriolis parameter is defined as $f = 2\Omega\sin\theta$. Similarly, the Northerly (θ) momentum equation (3) becomes,

$$v_t + \left(\frac{\epsilon}{\mu}\right)fu + \delta\left[\frac{u}{\cos\theta}v_{\phi^*} + vv_{\theta^*} + wv_z + \frac{\epsilon}{\mu}u^2\tan\theta\right]$$
$$+ \delta^{-1}p_{\theta^*} = O(\epsilon) \tag{22}$$

The dimensionless vertical momentum equation is finally given by

$$\delta\mu^2\left[w_t + \delta\left(\frac{u}{\cos\theta}w_{\phi^*} + vw_{\theta^*} + ww_z\right)\right] + (p_z + 1) = O(\epsilon) \tag{23}$$

In the following, we consider two relations between ϵ and μ: (1) the regime $\mu = O(\epsilon)$, which recovers the shallow water equations; and (2) the regime $\mu = O(\epsilon^{1/3})$, which yields the Boussinesq approximation. As a further note on the apparent scaling of the Coriolis parameter, f, consider the usual definition of the dimensional Rossby deformation radius $R' = \sqrt{gh'_0}/f' = \sqrt{gh'_0}/(2\Omega'\sin\theta)$. In the present scaling, we obtain $f = r'_0/R'$ or

$$\left(\frac{\epsilon}{\mu}\right)f = \frac{\lambda'}{R'} \tag{24}$$

which shows that the shallow water regime and Boussinesq regime can be thought of as covering waves which are $O(1)$ in length or much shorter than the Rossby deformation radius, respectively, the Coriolis effects being weaker in the latter case.

2.2. Shallow water equations

Most theories of transoceanic tsunami propagation are based on either the nonlinear shallow water equations (NSWE), or their linearized form, in recognition of the vanishing effects of dispersion ($\mu \to 0$) for very long waves. In the present discussion, this limit is obtained when the horizontal length scale of wave motion approaches the horizontal scale of a global-sized ocean basin, or $\lambda' \to r'_0$. This implies that the ratio $\epsilon/\mu = O(1)$, while terms proportional to μ appearing alone are essentially the size of already neglected terms of $O(\epsilon)$. In this combined limit, the local vertical momentum equation (23) reduces to a hydrostatic balance, which may be integrated down from the free surface to yield

$$p = \delta\eta - z \tag{25}$$

This expression is used to evaluate pressure gradient terms in the horizontal momentum equations, yielding the final set of shallow water equations

$$\frac{1}{\delta}H_t + \frac{1}{\cos\theta}[(H\overline{u})_\phi + (H\overline{v}\cos\theta)_\theta] = 0 \tag{26}$$

$$\overline{u}_t - f\overline{v} + \frac{\delta}{\cos\theta}[\overline{uu}_\phi + \cos\theta\overline{vu}_\theta - \sin\theta\overline{uv}] + \frac{1}{\cos\theta}\eta_\phi = 0 \tag{27}$$

$$\overline{v}_t + f\overline{u} + \frac{\delta}{\cos\theta}[\overline{uv}_\phi + \cos\theta\overline{vv}_\theta + \sin\theta\overline{u}^2] + \eta_\theta = 0 \tag{28}$$

where, in this limit, the scaled latitude and longitude revert to the original values. Eq. (26) retains the possibility of describing wave

generation through a bottom motion h_t, which appears at $O(1/\delta)$ since h' is scaled by h'_0 rather than wave amplitude. This is important for modeling time dependent tsunami sources, such as occur for large co-seismic events (e.g., Indian Ocean in 2004 or Tohoku in 2011) or for landslide tsunamis.

2.3. The Boussinesq approximation

We now wish to retain dispersive effects to leading order in the description of wave motion. Further, in order to provide a uniformly valid model which can be used to describe nonlinear wave evolution in shallow coastal margins as well as mainly linear evolution in the deep ocean basin, we will retain the mechanics of the fully nonlinear Boussinesq model framework, following the approach of Chen (2006) and Shi et al. (2012a) but working in the framework of rotating flow. As in those studies, we use horizontal velocity $\mathbf{u}_\alpha$ at a reference level z_α as the dependent variable as a means of providing more accurate frequency dispersion effects as well as for connecting the model more directly to local-scale models in Cartesian coordinates. In developing the model, we seek to retain terms to $O(\mu^2)$ without any truncation in orders of δ. This is in contrast to the classical Boussinesq approach, which would take $\delta = O(\mu^2)$ and truncate terms of $O(\delta^2, \delta\mu^2, \mu^4)$ and higher.

In the derivation, we retain the effect of an imposed bottom motion $h(\phi, \theta, t)$. The approximation is accompanied by the assumption that $\mu = O(\epsilon^{1/3})$. For $\epsilon = O(10^{-3})$, this implies a dispersion term $\mu = O(10^{-1})$, which would be reasonable for the usual surface wave problems. This choice of scaling then implies that $O(\epsilon/\mu) = O(\mu^2)$, indicating that Coriolis terms and undifferentiated advective acceleration terms are the same size as the leading-order deviation of the pressure term from a hydrostatic balance.

2.3.1. Pressure and vertical momentum

Pressure in the system being considered will deviate from hydrostatic by $O(\mu^2)$ amounts. Denoting this non-hydrostatic component by $\tilde{p}$, we write

$$p(\phi^*, \theta^*, z, t) = p_h(\phi^*, \theta^*, z, t) + \delta\mu^2\tilde{p}(\phi^*, \theta^*, z, t)$$
$$= \delta\eta - z + \delta\mu^2\tilde{p} \tag{29}$$

Introducing (29) in (23) and integrating up to the free surface (where $\tilde{p} = 0$) gives

$$\tilde{p}(z) = \int_z^{\delta\eta} w_t \, dz + \delta \int_z^{\delta\eta} \left[\frac{u}{\cos\theta} w_{\phi^*} + v w_{\theta^*} + w w_z\right] dz + O(\epsilon) \tag{30}$$

The weakly nonlinear approximation with $\delta/\mu^2 = O(1)$ would retain

$$\tilde{p}(z) = \int_z^0 w_t \, dz + O(\delta) \tag{31}$$

2.3.2. The vertical structure of velocities

In order to use (30) to evaluate horizontal pressure gradients, we need to establish a relation between w and components (u, v) through the continuity equation (15), which simplifies to

$$w_z + \frac{\mu}{\cos\theta}[u_{\phi^*} + (v\cos\theta)_{\theta^*}] = O(\epsilon) \tag{32}$$

Integrating (32) from $-h$ to z and using the bottom boundary condition gives

$$w(z) = -\frac{1}{\cos\theta}\frac{\partial}{\partial\phi^*}\left(\int_{-h}^z u \, dz\right) - \frac{1}{\cos\theta}\frac{\partial}{\partial\theta^*}\left(\int_{-h}^z v\cos\theta \, dz\right) - \frac{1}{\delta}h_t \tag{33}$$

We now follow Nwogu (1993) and Chen (2006) and express the horizontal velocities using Taylor series expansions about a reference depth z_α. This approach, together with the closure assumption that horizontal components of vorticity are zero at leading order, expressed through

$$u_z = \mu^2\frac{w_{\phi^*}}{\cos\theta} + O(\mu^4, \epsilon), \quad v_z = \mu^2 w_{\theta^*} + O(\mu^4, \epsilon) \tag{34}$$

leads to the following expressions for the velocity components,

$$u(z) = u_\alpha + \frac{\mu^2}{\cos\theta}\left\{(z_\alpha - z)A_{\phi^*} - \frac{1}{2}(z_\alpha^2 - z^2)B_{\phi^*}\right\} + O(\mu^4, \epsilon) \tag{35}$$

$$v(z) = v_\alpha + \mu^2\left\{(z_\alpha - z)A_{\theta^*} - \frac{1}{2}(z_\alpha^2 - z^2)B_{\theta^*}\right\} + O(\mu^4, \epsilon) \tag{36}$$

$$w(z) = -A - Bz \tag{37}$$

where

$$A = \frac{1}{\delta}h_t + \frac{1}{\cos\theta}\{(u_\alpha h)_{\phi^*} + (v_\alpha\cos\theta h)_{\theta^*}\},$$
$$B = \frac{1}{\cos\theta}\{(u_\alpha)_{\phi^*} + (v_\alpha\cos\theta)_{\theta^*}\} \tag{38}$$

The vertical vorticity associated with (35) and (36) is given by

$$\omega = \omega_0 + \mu^2\omega_2(z) + O(\mu^4, \epsilon) \tag{39}$$

with

$$\omega_0 = \frac{1}{\cos\theta}v_{\alpha\phi^*} - u_{\alpha\theta^*} \tag{40}$$

and

$$\omega_2 = \frac{1}{\cos\theta}\{[A_{\theta^*}z_{\alpha\phi^*} + B_{\theta^*}z_\alpha z_{\alpha\phi^*}] - [A_{\phi^*}z_{\alpha\theta^*} + B_{\phi^*}z_\alpha z_{\alpha\theta^*}]\}$$
$$- \frac{\tan\theta}{\cos\theta}\left\{A_{\phi^*}(z_\alpha - z) + B_{\phi^*}\left(\frac{z_\alpha^2}{2} - \frac{z^2}{2}\right)\right\}\frac{d\theta}{d\theta^*} \tag{41}$$

In contrast to the case in Cartesian coordinates, the $O(\mu^2)$ contribution to the vorticity here is depth dependent. In the Boussinesq regime, however, we have $d\theta/d\theta^* = \mu^2$ and thus the additional time-dependent term is of $O(\mu^4)$ overall, moving it outside the approximate equations developed here. We thus denote $\omega_2(z) = \tilde{\omega}_2 + \mu^2\hat{\omega}_2(z)$ and neglect $\hat{\omega}_2$ from further analysis.

2.3.3. Fully nonlinear Boussinesq equations

Fully nonlinear Boussinesq equations are obtained first by using the expressions (35)–(37) to evaluate the pressure field (30), giving

$$\tilde{p}(z) = \mu^2\left\{[D_\alpha A - \delta AB](z - \delta\eta) + [D_\alpha B - \delta B^2]\left(\frac{z^2 - (\delta\eta)^2}{2}\right)\right\} \tag{42}$$

where

$$D_\alpha() = ()_t + \delta\left\{\frac{u_\alpha}{\cos\theta}()_{\phi^*} + v_\alpha()_{\theta^*}\right\} \tag{43}$$

is a total derivative following the horizontal motion in the local tangent plane. Substitution of Eqs. (35)–(37) into the ϕ momentum equation (21) gives the approximate horizontal momentum equation

$$u_{\alpha_t} - \mu^2 f v_\alpha + \frac{1}{\cos\theta}\eta_{\phi^*} + \delta\left[\frac{u_\alpha u_{\alpha_{\phi^*}}}{\cos\theta} + v_\alpha u_{\alpha_{\theta^*}} - \mu^2 u_\alpha v_\alpha\tan\theta\right]$$
$$+ \mu^2[V_1^{(\phi)} + V_2^{(\phi)} + V_3^{(\phi)}(z)] = O(\mu^4, \epsilon) \tag{44}$$

where

$$V_1^{(\phi)} = \frac{1}{\cos\theta}\left\{\frac{z_\alpha^2}{2}B_{t\phi^*} + z_\alpha A_{t\phi^*} - \left[\left(\frac{\delta\eta^2}{2}\right)B_t\right]_{\phi^*} - [\delta\eta A_t]_{\phi^*}\right\} \tag{45}$$

$$V_2^{(\phi)} = \frac{\delta}{\cos\theta}\left\{\left(\frac{z_\alpha^2 - (\delta\eta)^2}{2}\right)\left[\frac{u_\alpha B_{\phi^*}}{\cos\theta} + v_\alpha B_{\theta^*}\right]\right.$$
$$\left. + (z_\alpha - \delta\eta)\left[\frac{u_\alpha A_{\phi^*}}{\cos\theta} + v_\alpha A_{\theta^*}\right] + \frac{1}{2}[A + \delta\eta B]^2\right\}_{\phi^*} \tag{46}$$

$$V_3^{(\phi)}(z) = -\delta v_\alpha \tilde{\omega}_2 - \delta\omega_0\left\{(z_\alpha - z)A_{\theta^*} + \left(\frac{z_\alpha^2 - z^2}{2}\right)B_{\theta^*}\right\} \tag{47}$$

Similarly, the θ momentum equation can be written as

$$v_{\alpha_t} + \mu^2 f u_\alpha + \eta_{\theta^*} + \delta\left[\frac{u_\alpha v_{\alpha_{\phi^*}}}{\cos\theta} + v_\alpha v_{\alpha_{\theta^*}} + \mu^2 u_\alpha^2 \tan\theta\right]$$
$$+ \mu^2[V_1^{(\theta)} + V_2^{(\theta)} + V_3^{(\theta)}(z)] = O(\mu^4, \epsilon) \tag{48}$$

where

$$V_1^{(\theta)} = \left\{\frac{z_\alpha^2}{2}B_{t\theta^*} + z_\alpha A_{t\theta^*} - \left[\left(\frac{\delta\eta^2}{2}\right)B_t\right]_{\theta^*} - [\delta\eta A_t]_{\theta^*}\right\} \tag{49}$$

$$V_2^{(\theta)} = \delta\left\{\left(\frac{z_\alpha^2 - (\delta\eta)^2}{2}\right)\left[\frac{u_\alpha B_{\phi^*}}{\cos\theta} + v_\alpha B_{\theta^*}\right] + (z_\alpha - \delta\eta)\left[\frac{u_\alpha A_{\phi^*}}{\cos\theta} + v_\alpha A_{\theta^*}\right]\right.$$
$$\left. + \frac{1}{2}[A + \delta\eta B]^2\right\}_{\theta^*} \tag{50}$$

$$V_3^{(\theta)}(z) = \delta u_\alpha \tilde{\omega}_2 + \frac{\delta\omega_0}{\cos\theta}\left\{A_{\phi^*}(z_\alpha - z) + B_{\phi^*}\left(\frac{z_\alpha^2 - z^2}{2}\right)\right\} \tag{51}$$

At this level of approximation, all z-dependence is contained in the dispersive terms V_3. In order to obtain a reduced-dimension, Boussinesq type system, we follow Chen (2006) and average (47) and (51) over depth to obtain the expressions

$$\overline{V}_3^{(\phi)} = -\delta v_\alpha \tilde{\omega}_2 - \delta\omega_0\left\{A_{\theta^*}\left(\frac{1}{2}z_\alpha^2 - \frac{1}{6}\left[(\delta\eta)^2 - \delta\eta h + h^2\right]\right)\right.$$
$$\left. + B_{\theta^*}\left(z_\alpha - \frac{1}{2}(\delta\eta - h)\right)\right\} \tag{52}$$

and

$$\overline{V}_3^{(\theta)} = \delta u_\alpha \tilde{\omega}_2 + \frac{\delta\omega_0}{\cos\theta}\left\{B_{\phi^*}\left(\frac{1}{2}z_\alpha^2 - \frac{1}{6}[(\delta\eta)^2 - \delta\eta h + h^2]\right)\right.$$
$$\left. + B_{\phi^*}\left(z_\alpha - \frac{1}{2}(\delta\eta - h)\right)\right\} \tag{53}$$

To complete the set of Boussinesq equations, the continuity equation (17) is written by expressing $\bar{u}$ and $\bar{v}$ in terms of u_α and v_α, giving

$$\frac{1}{\delta}H_t + \frac{1}{\cos\theta}\left\{M_{\phi^*}^{(\phi)} + (M^{(\theta)}\cos\theta)_{\theta^*}\right\} = O(\epsilon, \mu^4) \tag{54}$$

where the volume flux components in ϕ and θ are given by

$$M^{(\phi)} = H\left\{u_\alpha + \frac{\mu^2}{\cos\theta}\left[\left(z_\alpha + \frac{1}{2}(h - \delta\eta)\right)A_{\phi^*} + \left(\frac{z_\alpha^2}{2} - \frac{h^2 - h\delta\eta + (\delta\eta)^2}{6}\right)B_{\phi^*}\right]\right\}$$
$$M^{(\theta)} = H\left\{v_\alpha + \mu^2\left[\left(z_\alpha + \frac{1}{2}(h - \delta\eta)\right)A_{\theta^*} + \left(\frac{z_\alpha^2}{2} - \frac{h^2 - h\delta\eta + (\delta\eta)^2}{6}\right)B_{\theta^*}\right]\right\}$$
$$\tag{55}$$

2.3.4. Weakly nonlinear approximation

The standard weakly nonlinear Boussinesq approximation follows from the assumption that $\delta = O(\mu^2)$, leading to the immediate neglect of all terms of $O(\delta\mu^2)$ in Eqs. (44), (48) and (54). The resulting set of approximate momentum equations are given by

$$u_{\alpha_t} - \mu^2 f v_\alpha + \frac{1}{\cos\theta}\eta_{\phi^*} + \delta\left[\frac{u_\alpha u_{\alpha_{\phi^*}}}{\cos\theta} + v_\alpha u_{\alpha_{\theta^*}}\right] + \mu^2\widetilde{V}_1^{(\phi)}$$
$$= O(\mu^4, \delta\mu^2, \epsilon) \tag{56}$$

where

$$\widetilde{V}_1^{(\phi)} = \frac{1}{\cos\theta}\left\{z_\alpha A_{t_{\phi^*}} + \frac{z_\alpha^2}{2}B_{t_{\phi^*}}\right\} \tag{57}$$

and

$$v_{\alpha_t} + \mu^2 f u_\alpha + \eta_{\theta^*} + \delta\left[\frac{u_\alpha v_{\alpha_{\phi^*}}}{\cos\theta} + v_\alpha v_{\alpha_{\theta^*}}\right] + \mu^2\widetilde{V}_1^{(\theta)}$$
$$= O(\mu^4, \delta\mu^2, \epsilon) \tag{58}$$

where

$$\widetilde{V}_1^{(\theta)} = \left\{z_\alpha A_{t\theta^*} + \frac{z_\alpha^2}{2}B_{t\theta^*}\right\} \tag{59}$$

The approximate volume fluxes in (56) follow from (55) and are given by

$$M^{(\phi)} = Hu_\alpha + \frac{\mu^2}{\cos\theta}h\left[\left(z_\alpha + \frac{1}{2}h\right)A_{\phi^*} + \left(\frac{z_\alpha^2}{2} - \frac{h^2}{6}\right)B_{\phi^*}\right]$$
$$M^{(\theta)} = Hv_\alpha + \mu^2 h\left[\left(z_\alpha + \frac{1}{2}h\right)A_{\theta^*} + \left(\frac{z_\alpha^2}{2} - \frac{h^2}{6}\right)B_{\theta^*}\right] \tag{60}$$

We note that the scaling automatically eliminates the undifferentiated advective acceleration terms in (56) and (58). These terms are also absent in the weakly nonlinear model of Løvholt et al. (2008) but are retained in the model of Zhou et al. (2011).

3. Numerical approach

The fully nonlinear system described here provides a comprehensive model for studying tsunamis from the earliest stages of generation to the final stages of shoreline inundation and runup. As pointed out in Løvholt et al. (2008), there are possible advantages to the fully nonlinear system particularly in the study of the development of undular bores over shelf regions, where weakly nonlinear models are known to over-predict bore undulation heights (Wei et al., 1995). However, it is our usual practice to simulate nearshore propagation and inundation using the corresponding model system in Cartesian coordinates, as described in Shi et al. (2012a) and used recently in Grilli et al. (2012a). For simplicity, we illustrate the numerical implementation of the weakly nonlinear system (56)–(60) here and obtain a model which is suitable for the generation and propagation studies considered in the following examples.

Recent progress in the development of Boussinesq-type wave models using a combined finite-volume and finite-difference TVD schemes has shown robust performance of the shock-capturing method in simulating breaking waves and coastal inundation (Tonelli and Petti, 2009; Roeber et al., 2010; Shiach and Mingham, 2009; Erduran et al., 2005, and others). In this study, we applied the MUSCL-TVD scheme in space and a high-order Runge–Kutta scheme in time with adaptive time stepping.

3.1. Conservative form of governing equations

The numerical implementation is based on dimensional forms of the weakly nonlinear governing equations, augmented by terms representing bottom friction. We also neglect the direct generation of waves due to bottom motion. The model equations are given by

$$H_t + \frac{1}{r_0 \cos\theta} \left\{ (Hu_\alpha)_\phi + (Hv_\alpha \cos\theta)_\theta \right.$$
$$+ \frac{1}{r_0^2 \cos\theta} \left[h\left(\left(z_\alpha + \frac{1}{2}h\right)A_\phi + \left(\frac{z_\alpha^2}{2} - \frac{h^2}{6}\right)B_\phi \right) \right]_\phi$$
$$\left. + \frac{1}{r_0^2} \left[h\cos\theta \left(\left(z_\alpha + \frac{1}{2}h\right)A_\theta + \left(\frac{z_\alpha^2}{2} - \frac{h^2}{6}\right)B_\theta \right) \right]_\theta \right\} = 0 \tag{61}$$

$$u_{\alpha t} - f v_\alpha + \frac{1}{r_0 \cos\theta} u_\alpha u_{\alpha\phi} + \frac{1}{r_0} v_\alpha u_{\alpha\theta} + \frac{g}{r_0 \cos\theta} \eta_\phi$$
$$+ \frac{1}{r_0^2 \cos\theta} \left\{ z_\alpha A_{t\phi} + \frac{z_\alpha^2}{2} B_{t\phi} \right\} + \frac{C_d}{H} |\mathbf{u}_\alpha| u_\alpha$$
$$= 0 \tag{62}$$

$$v_{\alpha t} + f u_\alpha + \frac{1}{r_0 \cos\theta} u_\alpha v_{\alpha\phi} + \frac{1}{r_0} v_\alpha v_{\alpha\theta} + \frac{g}{r_0} \eta_\theta$$
$$+ \frac{1}{r_0^2} \left\{ z_\alpha A_{t\theta} + \frac{z_\alpha^2}{2} B_{t\theta} \right\} + \frac{C_d}{H} |\mathbf{u}_\alpha| u_\alpha = 0 \tag{63}$$

with

$$A = \frac{(hu_\alpha)_\phi + (hv_\alpha \cos\theta)_\theta}{\cos\theta}, \quad B = \frac{(u_\alpha)_\phi + (v_\alpha \cos\theta)_\theta}{\cos\theta} \tag{64}$$

and where C_d represents a drag coefficient. The system of Eqs. (61)–(63) corresponds to the Nwogu-type equations used in Løvholt et al. (2008). In order to apply the combined finite-volume and finite-difference schemes, the governing equations (61)–(63) are re-arranged to a conservative form following Shi et al. (2012) for the fully non-linear Boussinesq equations in Cartesian coordinates. We define

$$\begin{cases} \xi_1 = r_0 \cos\theta_0 (\phi - \phi_0) \\ \xi_2 = r_0 (\theta - \theta_0) \end{cases} \tag{65}$$

where (ϕ_0, θ_0) are the reference longitude and latitude, respectively. (ξ_1, ξ_2) represent coordinates in the longitude and latitude directions, respectively. The conservative form of (61)–(63) can be written as

$$\frac{\partial \mathbf{\Psi}}{\partial t} + \nabla \cdot \mathbf{\Theta}(\mathbf{\Psi}) = \mathbf{S} \tag{66}$$

where $\mathbf{\Psi}$ and $\mathbf{\Theta}(\mathbf{\Psi})$ are the vector of conserved variables and the flux vector function, respectively, and are given by

$$\mathbf{\Psi} = \begin{pmatrix} H \\ U \\ V \end{pmatrix}, \quad \mathbf{\Theta} = \begin{pmatrix} S_p P \mathbf{i} + Q \mathbf{j} \\ \left[\frac{S_p P^2}{H} + \frac{1}{2} S_p g(\eta^2 + 2\eta h) \right] \mathbf{i} + \frac{PQ}{H} \mathbf{j} \\ \frac{S_p PQ}{H} \mathbf{i} + \left[\frac{Q^2}{H} + \frac{1}{2} g(\eta^2 + 2\eta h) \right] \mathbf{j} \end{pmatrix} \tag{67}$$

where S_p is a spherical coordinate correction factor given by

$$S_p = \frac{\cos\theta_0}{\cos\theta} \tag{68}$$

$P = Hu_\alpha + hu_1$ and $Q = Hv_\alpha + hv_1$, in which (u_1, v_1) are defined by

$$u_1 = \left(z_\alpha + \frac{h}{2}\right) S_p \left[S_p (hu_\alpha)_{\xi_1\xi_1} + (hv_\alpha)_{\xi_1\xi_2} - \frac{1}{r_0} \tan\theta (hv_\alpha)_{\xi_1} \right]$$
$$+ \left(\frac{z_\alpha^2}{2} - \frac{h^2}{6}\right) S_p \left[S_p u_{\alpha\xi_1\xi_1} + v_{\alpha\xi_1\xi_2} - \frac{1}{r_0} \tan\theta v_{\alpha\xi_1} \right] \tag{69}$$

$$v_1 = \left(z_\alpha + \frac{h}{2}\right) \left[S_p (hu_\alpha)_{\xi_1\xi_2} + (hv_\alpha)_{\xi_2\xi_2} - \frac{1}{r_0} (\tan\theta hv_\alpha)_{\xi_2} \right]$$
$$+ \left(\frac{z_\alpha^2}{2} - \frac{h^2}{6}\right) \left[S_p u_{\alpha\xi_1\xi_2} + v_{\alpha\xi_2\xi_2} - \frac{1}{r_0} (\tan\theta v_\alpha)_{\xi_2} \right] \tag{70}$$

The conserved variables U and V in (67) are given by

$$U = H(u_\alpha + F) \tag{71}$$

$$V = H(v_\alpha + G) \tag{72}$$

in which

$$F = \frac{z_\alpha^2}{2} S_p^2 u_{\alpha\xi_1\xi_1} + \frac{z_\alpha^2}{2} S_p \left(v_{\alpha\xi_1\xi_2} - \frac{1}{r_0} \tan\theta v_{\alpha\xi_1} \right) + z_\alpha S_p^2 (hu_\alpha)_{\xi_1\xi_1}$$
$$+ z_\alpha S_p \left[(hv_\alpha)_{\xi_1\xi_2} - \frac{1}{r_0} \tan\theta (hv_\alpha)_{\xi_1} \right] \tag{73}$$

and

$$G = \frac{z_\alpha^2}{2} (S_p u_{\alpha\xi_1})_{\xi_2} + \frac{z_\alpha^2}{2} \left(v_{\alpha\xi_2\xi_2} - \frac{1}{r_0} (\tan\theta v_\alpha)_{\xi_2} \right)$$
$$+ z_\alpha [S_p (hu_\alpha)_{\xi_1}]_{\xi_2} + z_\alpha \left[(hv_\alpha)_{\xi_2\xi_2} - \frac{1}{r_0} (\tan\theta hv_\alpha)_{\xi_2} \right] \tag{74}$$

$\mathbf{S}$ in (66) represents a source array given by

$$\mathbf{S} = \begin{pmatrix} \frac{1}{r_0} \tan\theta (Hv_\alpha + hv_1) \\ S_p g\eta \frac{\partial h}{\partial \xi_1} + fHv_\alpha - C_d u_\alpha \sqrt{u_\alpha^2 + v_\alpha^2} + \psi_1 \\ g\eta \frac{\partial h}{\partial \xi_2} - fHu_\alpha - C_d v_\alpha \sqrt{u_\alpha^2 + v_\alpha^2} + \psi_2 \end{pmatrix} \tag{75}$$

where

$$\psi_1 = \eta_t (F - u_1) + h(S_p u_\alpha u_{1\xi_1} + v_\alpha u_{1\xi_2} + S_p u_1 u_{\alpha\xi_1} + v_1 u_{\alpha\xi_2}) \tag{76}$$

$$\psi_2 = \eta_t (G - v_1) + h(S_p u_\alpha v_{1\xi_1} + v_\alpha v_{1\xi_2} + S_p u_1 v_{\alpha\xi_1} + v_1 v_{\alpha\xi_2}) \tag{77}$$

The surface elevation gradient term was split into $(\frac{1}{2} S_p g(\eta^2 + 2\eta h), \frac{1}{2} g(\eta^2 + 2\eta h))$ in (67) and $(S_p g\eta h_{\xi_1}, g\eta h_{\xi_2})$ in (75) in order to use a well-balanced numerical scheme (Shi et al., 2012a).

Eq. (66) is solved using the MUSCL-TVD scheme and the HLL approximate Riemann solver. A MUSCL-TVD scheme up to the fourth-order in space (Yamamoto and Daiguji, 1993) and a third-order Strong Stability-Preserving (SSP) Runge–Kutta (Gottlieb et al., 2001) in time were adopted. Model implementation also includes wave breaking and wetting–drying schemes for shallow water, as described in Shi et al. (2012a).

3.2. Parallelization

In parallelizing the computational model, we use the domain decomposition technique to subdivide the problem into multiple regions and assign each subdomain to a separate processor core. Each subdomain region contains an overlapping area of ghost cells three rows deep, as dictated by the 4th order computational stencil for the leading order non-dispersive terms. The Message Passing Interface (MPI) with non-blocking communication is used to exchange data in the overlapping region between neighboring processors. Velocity components are obtained from Eqs. (46) and (47) by solving tridiagonal matrices using the parallel pipelining tridiagonal solver described in Naik et al. (1993).

To investigate the performance of the parallel program, numerical simulations of an idealized ocean case were first tested with different numbers of processors on the linux cluster mills.hpc.udel.edu using a heterogeneous set of nodes consisting of nodes with 24–2.4 GHz cores and 64 GB of memory or 48–2.4 GHz cores and 128 GB of memory per node. Tests here were conducted using 24 core nodes. The test case uses a numerical grid of dimension 5400×3600. Fig. 2 shows the model speedup versus number of processors for tests with 1, 8, 16, 24, 36, 48 and 64 processors. The effect of inter-node communication is noted as the computation moves from one to two nodes (above 24 processors) and from two to three nodes (above 48 processors), but overall performance
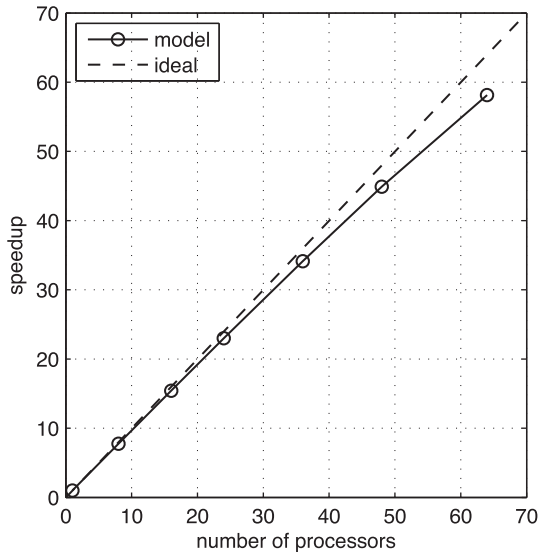
Fig. 2. Variation in model performance with number of processors for a 5400×3600 domain. Straight line indicates arithmetic speedup. Actual performance shown by circles.

is satisfactory in comparison to an ideal arithmetic speedup based on performance using a single processor.

4. Tests of dispersion and Coriolis effects

The orders of the frequency dispersions terms and Coriolis terms in Eqs. (47) and (48) are $O(\mu^2)$ and $O(\epsilon/\mu)$, respectively. The relative importance of frequency dispersion and Coriolis force can be evaluated using μ^2 and ϵ/μ values in some specific cases. Fig. 3 illustrates variations of μ^2 and ϵ/μ with respect to μ or h_0/W, where W represents the characteristic width of the tsunami source. Typically, for a source width of 100 km (for example, the 2004 Indian Ocean tsunami), $\mu \approx 0.025$ and the Coriolis effect would be expected to be relatively more important than dispersion as shown in Fig. 3. This result would apply to all co-seismic sources with widths in the range $50 \leqslant W \leqslant 500$ km, for which $0.01 \leqslant \mu \leqslant 0.1$. For narrower sources with widths on the order of 25 km or less, μ values lie to the right of the intersection point in
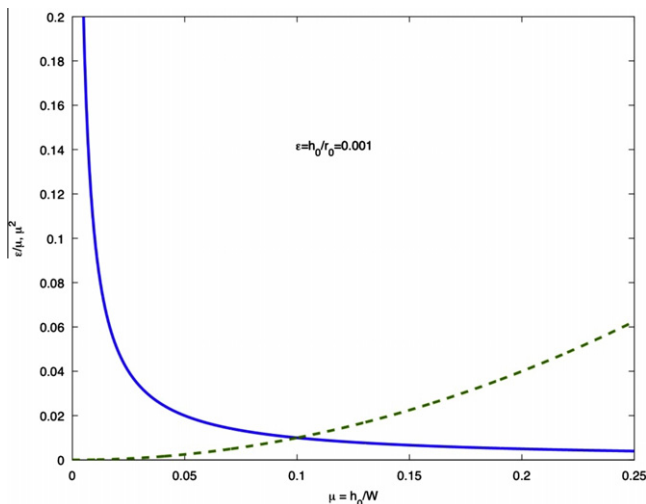
Fig. 3. Relative importance of Coriolis force (ϵ/μ) and frequency dispersion (μ^2) with varying inverse source width $\mu = h_0/W$.
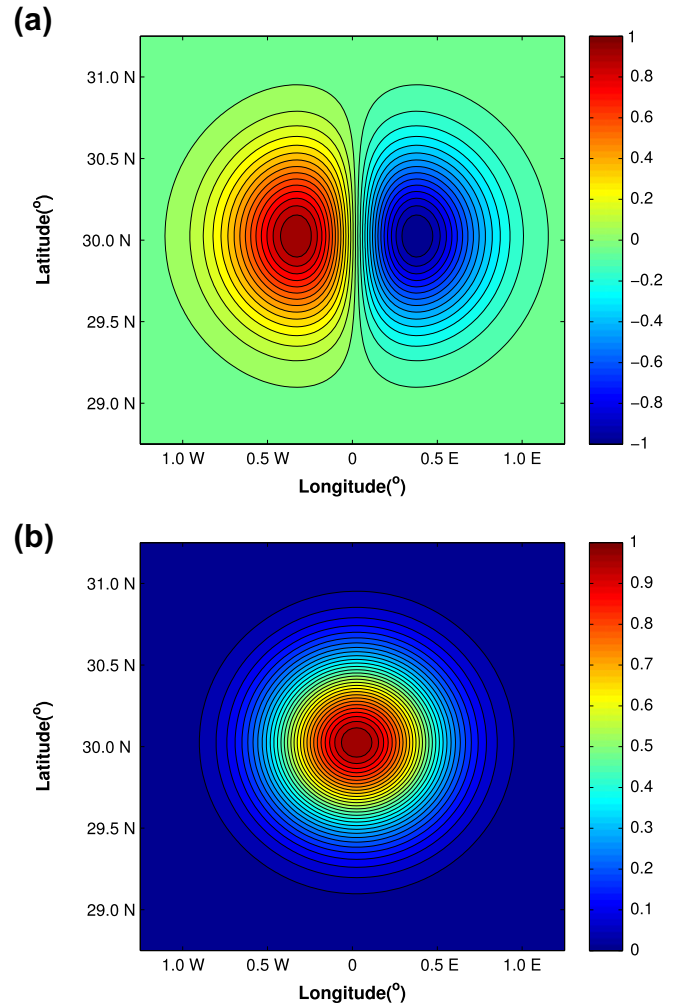
Fig. 4. Geometries for (a) a dipolar source and (b) a Gaussian source used in model testing.

Fig. 3, indicating that dispersive effects are as important as the Coriolis effect, and get relatively more important as the source width diminishes. Nevertheless, in the examples considered below, we find that Coriolis effects are uniformly less important than dispersion effects for all the cases considered, even though the scaling indicates otherwise.

4.1. Idealized tsunami sources and examples

There is a significant lack of benchmark examples that can be used as test cases for the determination of accuracy of spherical coordinate ocean wave models. Shi et al. (2012b) have described the testing of an earlier version of the present code, based on depth-averaged velocity, against the standard tsunami benchmark tests provided by Synolakis et al. (2007). Here, we compare model results to several of the detailed measurements obtained from DART buoys during the 2011 Tohoku-oki tsunami event. Before turning to the realistic example, we first illustrate the dependence of the maximum wave height envelope on the effect of dispersive and Coriolis effects using idealized sources which may be taken to be indicative either of localized SMF events or of co-seismic events with limited lateral extent.

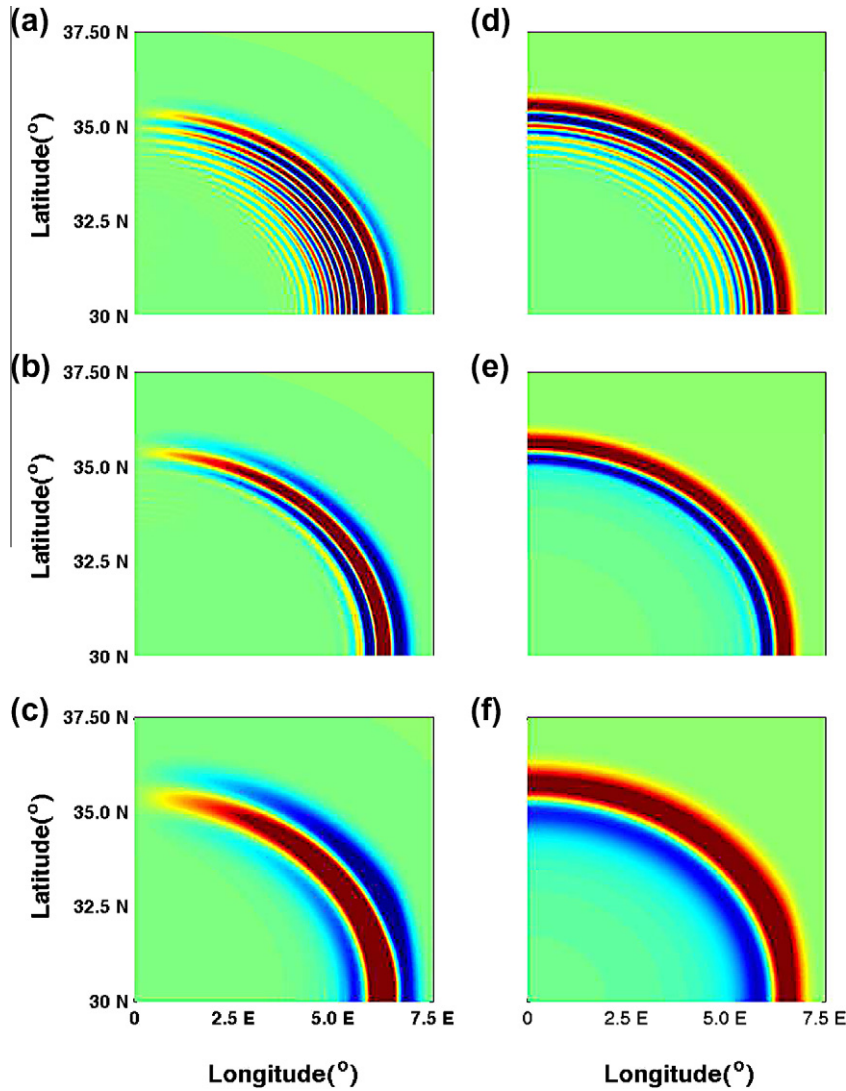We utilize two idealized sources here: an initial Gaussian elevation

Fig. 5. (a) Dipolar initial condition ($W = 0.25°$, $P_a = 2.5$), (b) dipolar initial condition ($W = 0.5°$, $P_a = 5.0$), (c) dipolar initial condition ($W = 1.0°$, $P_a = 10.0$), (d) Gaussian initial condition ($W = 0.25°$, $P_a = 2.5$), (e) Gaussian initial condition ($W = 0.5°$, $P_a = 5.0$), and (f) Gaussian initial condition ($W = 1.0°$, $P_a = 10.0$), $T = 5000$ s.

$$\eta(\phi, \theta) = A \exp\left[-\frac{r_0^2}{W^2}((\phi - \phi_c)^2 + (\theta - \theta_c)^2)\right] \quad (78)$$

with center at (ϕ_c, θ_c), nominal source width W and amplitude A, and a dipolar initial displacement given by

$$\eta(\phi, \theta) = \frac{2\sqrt{2}}{W} r_0(\phi - \phi_c) \exp\left[-\frac{r_0^2}{W^2}((\phi - \phi_c)^2 + (\theta - \theta_c)^2)\right] \quad (79)$$

where the orientation of the dipole may be changed by altering the first $(\phi - \phi_c)$ factor. The shapes of these initial forms are shown in Fig. 4. Of these two, the dipolar source is most representative of tsunami-like sources, and could represent either the net upward and downward displacement of an Okada-like source, or the net effect of lateral translation or rotation of an SMF event.

We consider an idealized ocean and use a model grid in spherical coordinates with a flat bottom bathymetry over the entire ocean basin. The computational domain is in the northern hemisphere and covers a region from 10°N to 50°N in the south-north direction and from 20°W to 20°E in the west-east direction. Water depth $h = 3000$ m over the whole domain. The grid resolution is $0.75'$. As is classically done in tsunami analyses, the bottom deformation is transferred to the spherical Boussinesq model as an

initial free surface condition with no initial fluid velocities, specified by either (78) or (79).

4.2. Source size and wave dispersion effect

The first set of examples considers the effect of varying source with on the rate of appearance of dispersive effects, using both of the source configurations considered above. Results are analyzed in light of a parameter due to Kajiura (1963), given by

$$P_a = \left(\frac{6h}{L}\right)^{1/3}\left(\frac{W}{h}\right) \quad (80)$$

where h is ocean depth, W is source width (as an indicator of basic wavelength), and L denotes travel distance. Kajiura indicates that dispersive effects should begin to become apparent when the value of the P_a, which decreases with travel distance, drops below 4.

Fig. 5 shows a snapshot at time $t = 5000$ s of the NE quadrant of wave trains evolving from both sources (78) and (79) with varying source widths. Panels (a)–(c) correspond to a dipolar source oriented in the E–W direction, while panels (d)–(f) correspond to Gaussian sources. Panels (a) and (d) correspond to a narrow initial
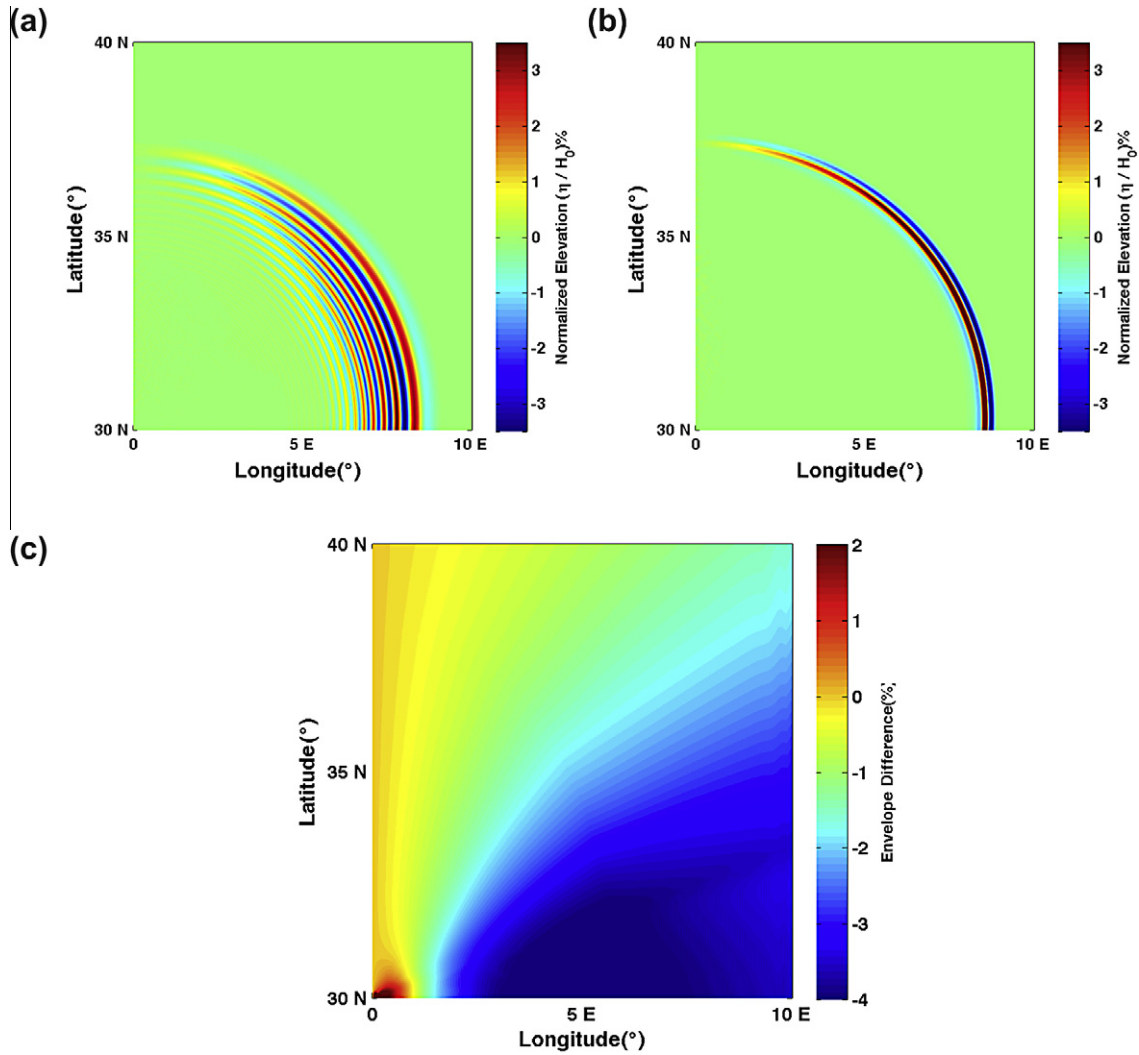
Fig. 6. Dipolar initial condition with E–W orientation and $W = 0.25°$. (a) With dispersive terms, $P_a = 2.5$, $t = 5000$ s; (b) without dispersive terms, $P_a = 2.5$, $t = 5000$ s; (c) difference in wave height envelope, dispersive–nondispersive. Plots are in percent of maximum initial displacement, equal to 1 m.

source with $W = 0.25°$, corresponding to an SMF-sized source with a width of about 25 km, with parameter $P_a = 2.5$, indicating the strong evolution of a dispersive wave train at the time of 1.4 h after event initiation. In contrast the lower panels (c) and (f) represent a source with initial width $W = 1°$ or about 100 km, consistent with a larger co-seismic slip event. At this elapsed time of 1.4 h, $P_a \sim 10$ and dispersive effects are not apparent, indicating that dispersion (as manifested by the presence of an oscillatory wave train) is not likely to occur for the first several hours during the evolution of a wave train from a classic co-seismic event.

Figs. 6 and 7 show the effect of dispersion on the spatial pattern of maximum wave height for a strongly dispersive case. Fig. 6(a) and (b) shows the wave fields at $t = 5000$ s for dispersive and non-dispersive calculations, respectively, for the dipolar source with initial $W = 0.25°$, corresponding to Fig. 5(a). Fig. 6(c) shows the spatial pattern of the difference in wave height envelope for the simulations with and without dispersion, and shows that there is a general tendency towards a decrease in wave height along the principle propagation direction when dispersion is taken into account. (This tendency also occurs in the realistic simulations of the Tohoku-oki event shown below, although the tendency is reversed at distances which are relatively shorter (higher P_a) than

the distances considered here, possibly due to complex refraction/diffraction effects over the variable ocean bathymetry.) Similar results occur for the Gaussian source as indicated in Fig. 7, aside from a more uniform distribution of results due to the initially symmetric source.

Figs. 8 and 9 provide a more detailed picture of the evolution of the dispersive wave train evolving from the dipolar or Gaussian sources respectively, with $W = 0.25°$ in either case. In each panel (a)–(f), a distance $D = \sqrt{ght}$ along an E–W transect through the source center is chosen, and then a time series of the resulting wave form passing that point is constructed with the time axis shifted by the amount t, to obtain an arrival time of zero for a non-dispersive wave in Cartesian coordinates. In each figure, the distance of the measurement point from the source origin along the E–W direction varies from 308.6 km (at top) to 1851.8 km (at bottom), corresponding to values of P_a falling from 3.11 to 1.71. In this case, frequency dispersion is seen to be important at all displayed distances from the source, and the evolved wave train represents an extensive packet of waves with a gradually decreasing wave period as the wave passes a fixed point, indicting the expected sorting of longer and shorter waves due to phase speed dependence on frequency.
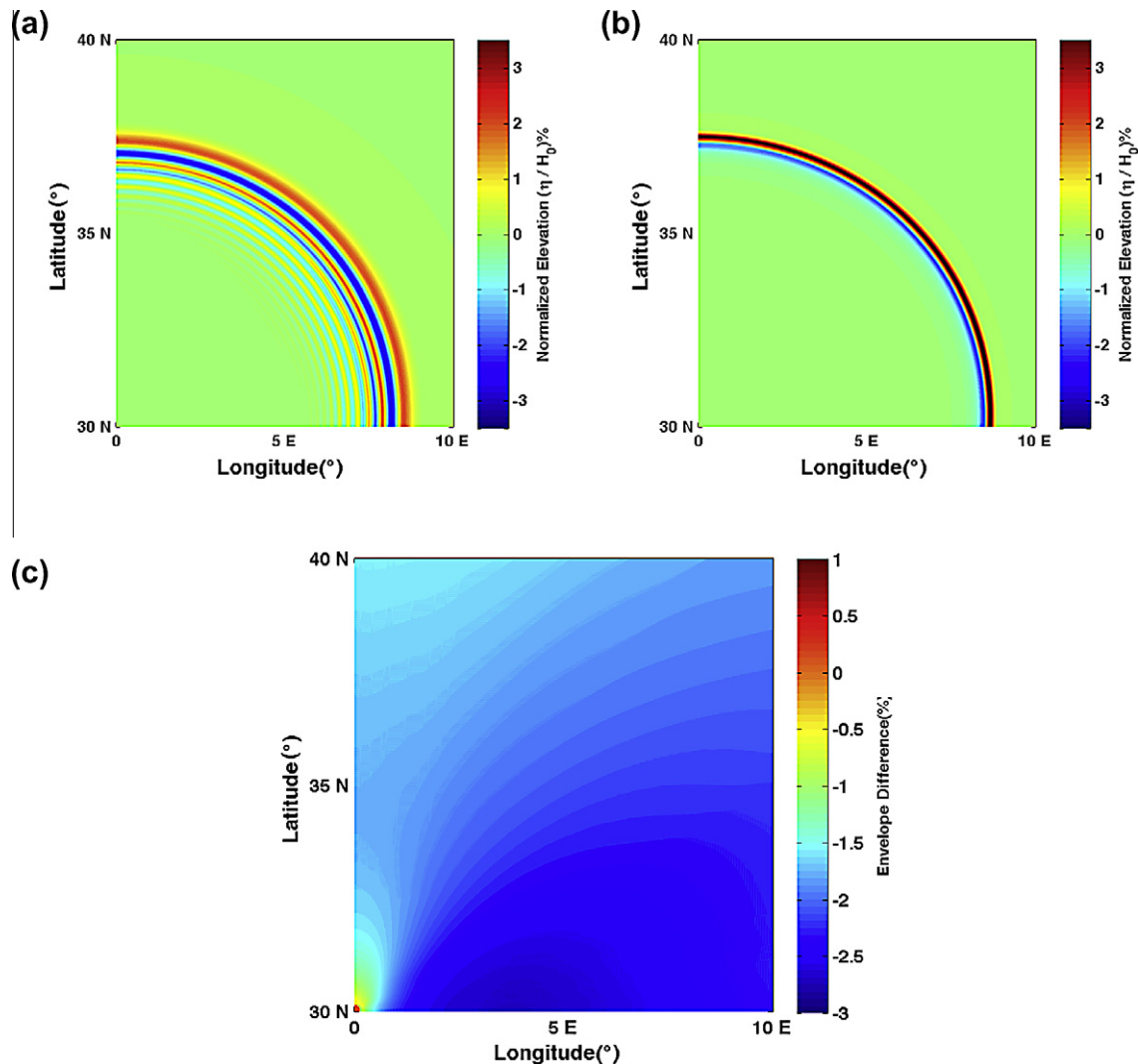
Fig. 7. Gaussian initial condition with $W = 0.25°$. (a) With dispersive terms, $P_a = 2.5$, $t = 5000$ s; (b) without dispersive terms, $P_a = 2.5$, $t = 5000$ s; (c) difference in wave height envelope, dispersive–nondispersive. Plots are in percent of maximum initial displacement, equal to 1 m.

4.3. Coriolis effect on an idealized source

The examples presented in the previous section included Coriolis effects in the computations. Corresponding runs without Coriolis were found to have only minor effects on the outcome, in line with the case study of the Tohoku-oki event discussed in the following section. In this section, we consider an additional idealized case of a dipolar source centered at 50°N with a N–S orientation. This latitude corresponds to Aleutian Island sources, and is chosen so as to give a source located in a region with elevated rotational effects. The source considered here has a width $W' = 4°$ or about 300 km, which is still considerably smaller than an estimate of the Rossby radius of deformation of 1800 km for a water depth of $h' = 4$ km and this latitude. Correspondingly, Coriolis effects on the solution are still weak at this latitude. Fig. 10 illustrates a comparison of the maximum wave height envelope after 10 h of simulation for cases with and without Coriolis included, with solid contours corresponding to the case with Coriolis and dashed contours corresponding to the case without. Contour levels correspond to percentage of the initial source height. Coriolis is seen to lead to a somewhat more rapid decay of the wave height with distance form the source center. The results also indicate that the results with Coriolis are somewhat asymmetrical in the E–W direction,

with wave heights being larger to the East, or left, of the main direction of propagation. This is a seemingly paradoxical result, as we may expect the tendency of Coriolis to deflect motions to the right in the Northern hemisphere to cause greater wave heights to the right of the propagation direction, as illustrated in the next section for the Tohoku-oki event. In order to examine this further, we consider an idealized case of diplolar sources with N–S and E–W orientation with Coriolis either included or neglected. The source geometry and latitude are unchanged. Fig. 11(a) and (b) display results with and without Coriolis force included for the same case as in Fig. 10. Fig. 11(c) shows the difference between run with Coriois (a) and the run without Coriolis (b). The most obvious effect noted here is that Coriolis tends to trap a portion of the initial wave close to its original position, leading to a persistent dipolar feature near the source center at (50°N, 0°E). The pattern also indicates that the evolving wave form with Coriolis is somewhat lower in amplitude to the right of the Southerly propagation direction, in agreement with Fig. 10. The waveform with Coriolis also has a lower amplitude at the leading edge of the spreading wave, indicating that Coriolis is reducing wave propagation speed to a small extent. The dipolar source with E–W orientation (Fig. 11(d)–(f)) also shows a reduction in wave speed induced by Coriolis and a tendency to trap a portion of the initial wave form near the source location.
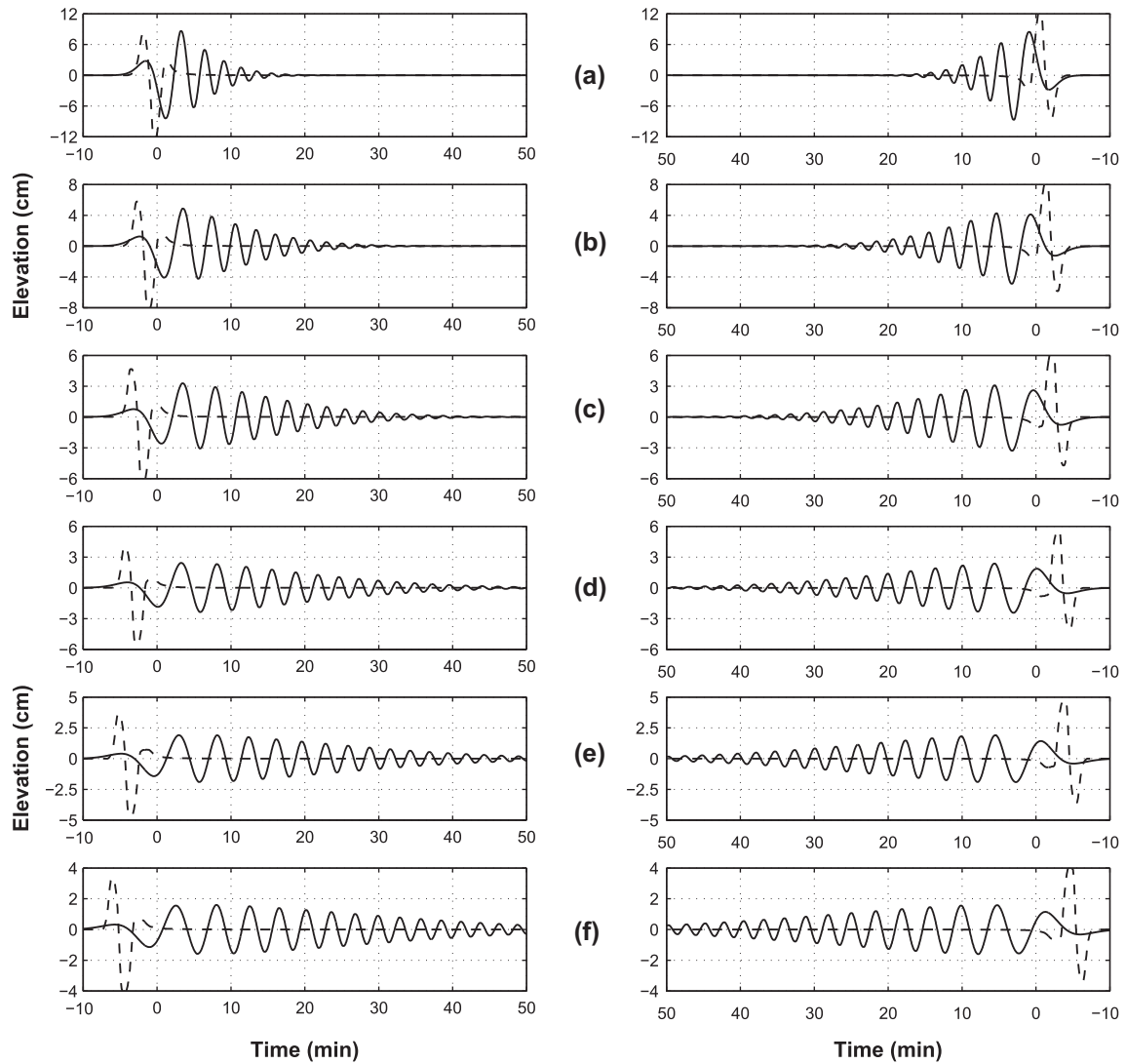
Fig. 8. Evolution of dispersive (solid line) and nondispersive (dashed line) wave trains for a dipolar source with initial width $W = 0.25°$. Left and right panels show westward and eastward propagating waves, respectively. Measurement locations are at $D = \sqrt{ght}$ with $h = 3000$ m and t, $D =$ (a) 1800 s and 308.6 km; (b) 3600 s and 617.3 km; (c) 5400 s and 925.8 km; (d) 7200 s and 1234.5 km; (e) 9000 s and 1543.1 km; and (f) 10,800 s and 1851.8 km.

At the propagation distances shown here, there is no clear tendency for the evolving waves to be deflected to the right or left of the principle propagation direction. See the following section for indications of this sort of behavior for much larger propagation distances in a realistic event.

Overall, the effect of Coriolis terms on evolving tsunami wave fronts appears to be of minimal importance, as noted in a number of earlier investigations (Kowalik et al., 2005; Løvholt et al., 2008).

4.4. The 2011 Tohoku-oki tsunami

The ability of the new spherical Boussinesq model to simulate basin-scale tsunami events is demonstrated in this section by applying the model to the recent March 11th, 2011 M9 Tohoku-oki earthquake. During this event, an extremely devastating tsunami was generated in the near-field while a significant tsunami was observed at many far-field locations. Grilli et al. (2012a) provide a detailed account of the event, the earthquake source, the near- and far-field tsunami observations, and tsunami generation and propagation modeling using both the Cartesian version (Shi et al., 2012a) and an earlier spherical version of FUNWAVE-TVD based on depth-averaged velocity. Here, we present results of sim-

ulations with the weakly-nonlinear spherical Boussinesq model described above. We specifically analyze effects of dispersion and Coriolis terms in the model equations on simulated maximum tsunami elevation in the Pacific Ocean. Comparisons are made based on measured and modeled time series at the location of four DART buoys, one near Japan (21418), one off Oregon (46404), one near Hawaii (51407), and one near Panama (32411) as shown in Fig. 14, and on a comparison of synoptic maps of maximum wave height envelopes for the entire Pacific basin.

As in Grilli et al. (2012a), the computational domain covers a region of the Pacific Ocean from 60°S to 60°N in the south-north direction, and from 132°E to 68°W in the west-east direction (Fig. 12). In the present simulations, the grid resolution is improved to 2′ compared to the 4′ resolution used in Grilli et al. (2012a). Bathymetry is specified in the model based on the ETO-PO1 1′ data base. In these simulations, we use the tsunami source of Grilli et al. (2012a), which is based on the 3D FEM model of Masterlark (2003). This source, denoted UA, was derived from a combination of seismic and GPS inversion to specify the earthquake-induced bottom uplift or subsidence as a function of time. The model simulations here do not make use of any hydrodynamic data in the determination of the source configuration.
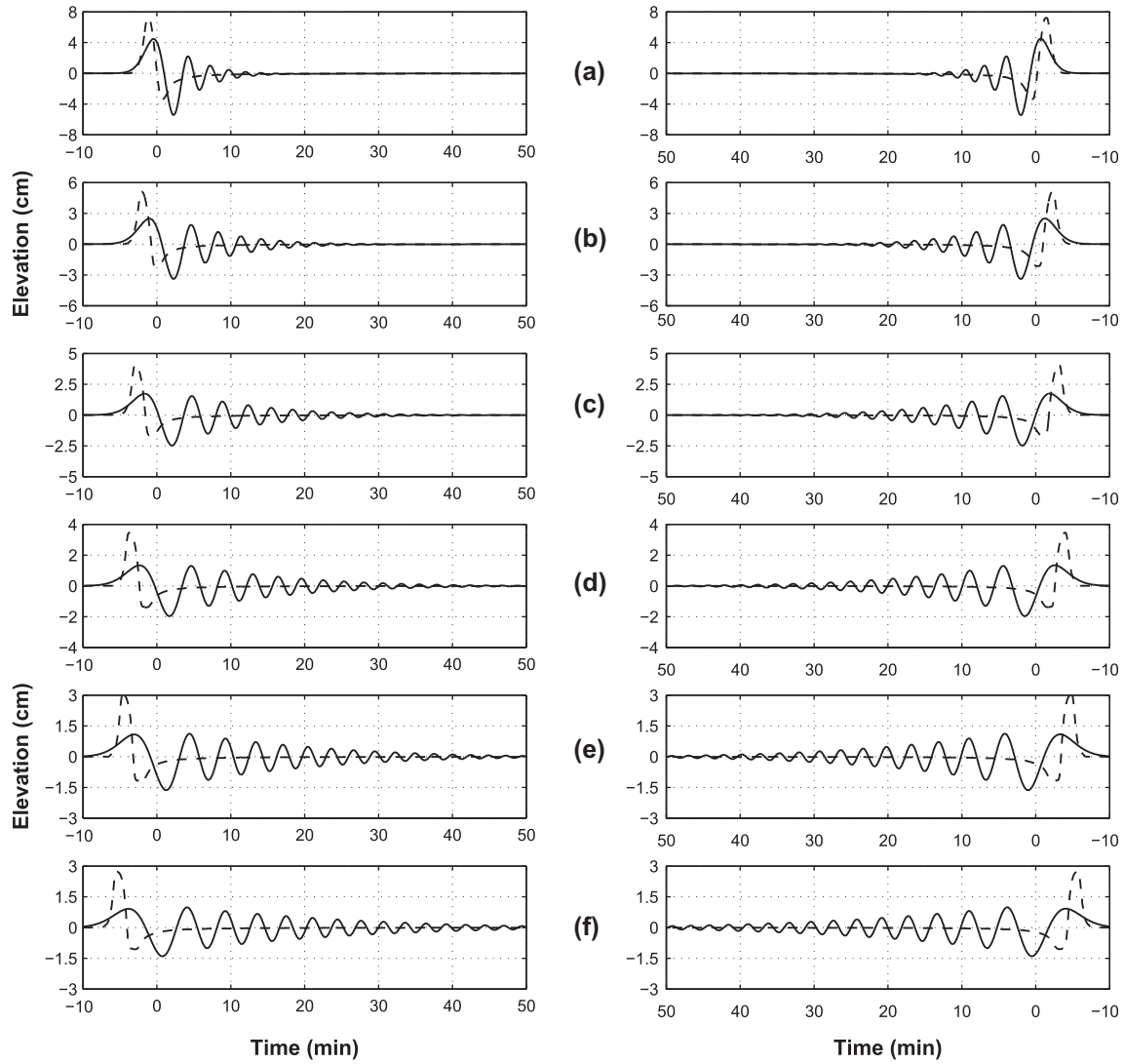
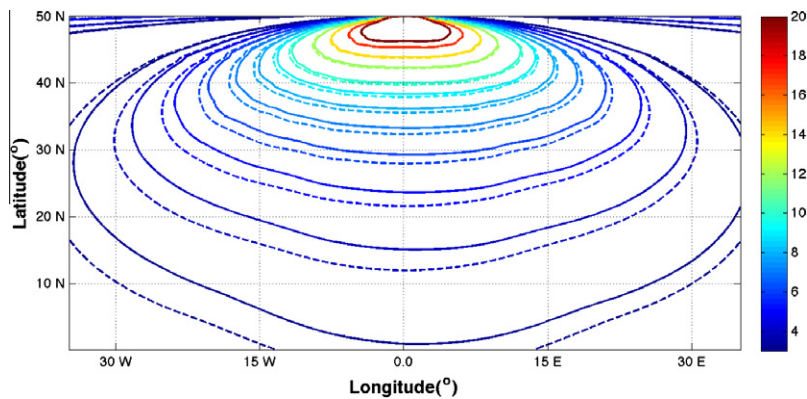**Fig. 9.** Gaussian source, parameters as in Fig. 8.

Fig. 10. (a) Comparison maximum recorded surface elevation (relative to initial source amplitude) with Coriolis (solid lines) and without Coriolis (dashed lines) after 10 h of simulated time. Dipolar source with width $W' = 4.0°$) oriented in North–South direction.

The non-hydrostatic model NHWAVE (Ma et al., 2012) is used to simulate the first 5 min of tsunami generation, as in Grilli et al. (2012a), using a smaller and finer local 1 km resolution Cartesian grid (see red rectangle in Fig. 12), based on the UA source.

NHWAVE results for surface elevation and depth-averaged horizontal velocity at $t = 5$ min are then interpolated over the spherical Boussinesq model grid, in which computations are then initiated as a hot start. For a more detailed description of model
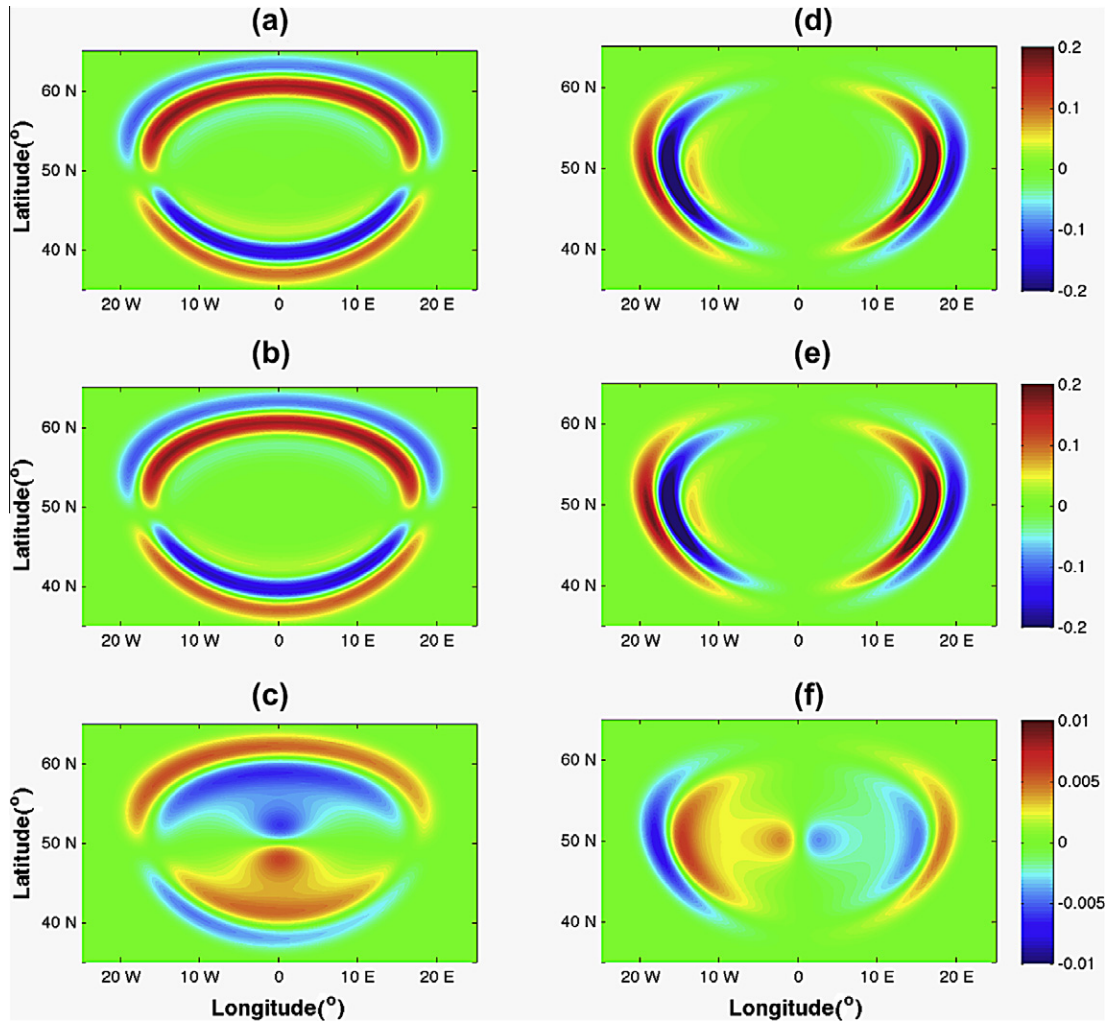
Fig. 11. Surface elevation comparison at $T = 7200$ s for dipolar sources with initial width $W = 4°$ and (a) North–South orientation with Coriolis, (b) North–South orientation without Coriolis, (c) (a,b), (d) East–West orientation with Coriolis, (e) East–West orientation without Coriolis, and (f) (d,e).
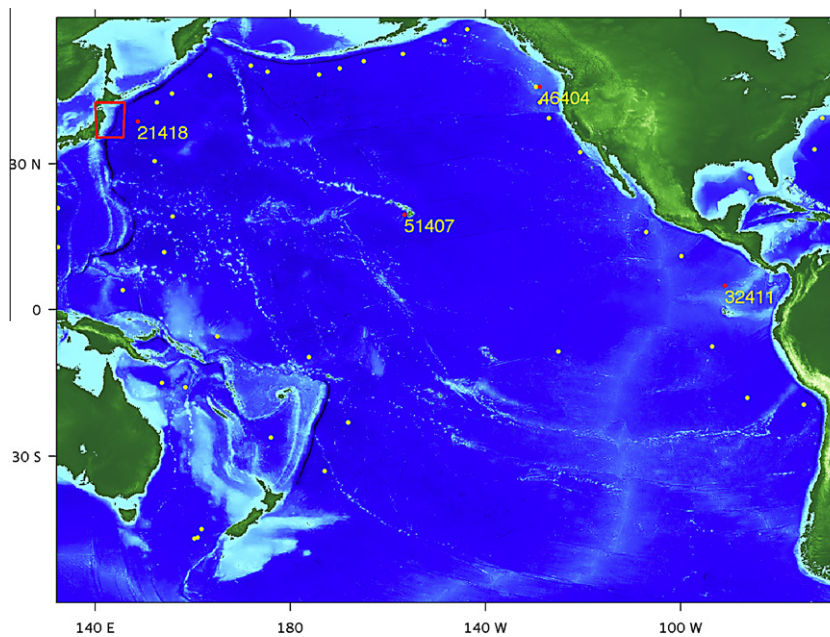

Fig. 12. Computational domain for far-field simulations with FUNWAVE-TVD, with the marked location of all DART buoys in the region (labeled red dots used in comparisons). The smaller red box marks the location of NHWAVE's regional computational domain (Grilli et al., 2012a,b). (For interpretation of the references to color in this figure legend, the reader is referred to the web version of this article.)
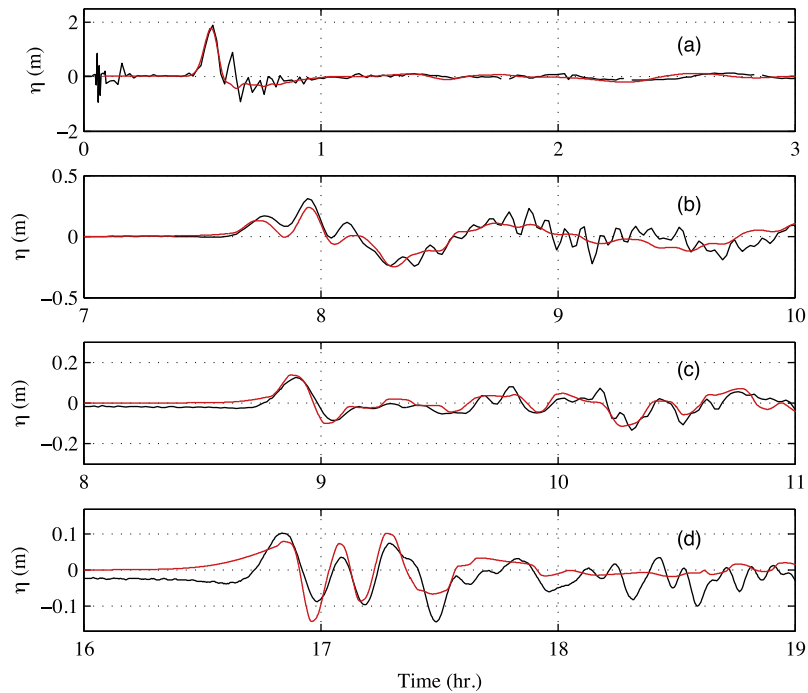
Fig. 13. Comparison between measured surface elevation at DART buoys (black) and model simulations using full model including dispersion and Coriolis effects. Simulations are based on the seismic/GPS UA source described in Grilli et al. (2012a). Buoy numbers and lead in model arrival time are (a) 21418, 0 min; (b) 51407, + 5 min; (c) 46404, + 6 min, and (d) 32411, +10 min. Model results are offset by the indicated shift to facilitate wave form comparisons.

setup, as well as a more comprehensive comparison of observations and model results based on the depth-averaged velocity formulation, see Grilli et al. (2012a).

Fig. 13 shows a comparison of DART buoy measurements and full model predictions (retaining dispersion and Coriolis) at the four selected locations. Timing of arrival of the main tsunami peak

at the nearest buoy 21418 is accurate, and the wave form is reproduced accurately aside from a trailing high frequency wave train that follows the main peak in the observations. (Grilli et al. (2012b) have recently speculated that the primary source of this early manifesting, shorter period (3–4 min) wave train is an SMF source located to the north of the main coseismic slip.) Using an
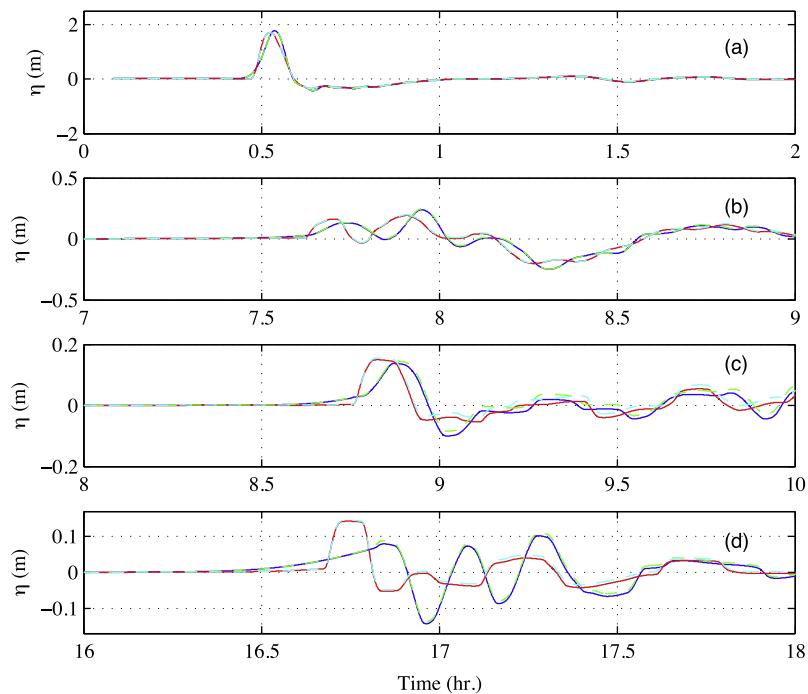

Fig. 14. Model predicted surface elevations at DART buoys: (a) 21418, (b) 51407, 46404, and (d) 32411. Full model (blue line), no dispersion (red line), no Coriolis (blue dashed line), and no dispersion/Coriolis (green dashed line). (For interpretation of the references to color in this figure legend, the reader is referred to the web version of this article.)

estimated source width $W' = 100$ km and an average depth of $h' = 4$ km, an estimated travel distance of 1300 km at buoy 21418 gives a value $P_a = 6.6$, indicating that dispersive effects should not be apparent for waves generated by the main co-seismic source. At more distant buoys, the model results lead the measurements in arrival timing, with a progressive increase in lead time with distance from the initial event source. Approximate lead times are 300 s at 51407, 360 s at 46404, and 600 s at 32411. This timing discrepancy could be due to a number of factors, including deviations from sphericity, errors in bathymetry, errors in leading order model dispersion, and truncation errors associated with discretization. We have not done simulations at a higher resolution of 1 min in order to test convergence, but note that results at 2 min resolution are significantly improved over results at 4 min resolution, where timing discrepancies are larger (Grilli et al., 2012a).

Fig. 13(b)–(d) display model results with the leading shift in time removed in order to facilitate comparisons of the modeled wave forms. The results at the three distant buoys indicate that the model accurately predicts the evolution of the leading features of the tsunami wave train, with good reproduction of the sequence, period and amplitudes of arriving wave crests.

The effects of Coriolis force and frequency dispersion are illustrated by comparing numerical results obtained with and without each term in the model equations in Fig. 14. Fig. 14(a) shows that the effect of frequency dispersion on the wave train is significant already at buoy 21418, where a forward steepening of the nondispersive wave form is apparent in comparison to the wave form with dispersion retained, although no oscillatory dispersive tail has appeared yet. The differences between dispersive and nondispersive calculations increase with distance from the source, and, by the farthest buoy 32411, dispersion has created a wave train with significant following crests that are largely absent in the nondispersive case, as would be expected. The parameter P_a takes on approximate values of 3.9, 3.7 and 3.0 at buoys 51407, 46404 and 32411, respectively, indicating that dispersive effects should only be mildly apparent at the two intermediate buoys, and relatively more apparent at the most distant buoy, as is seen in the model results. In contrast, the figure shows that the effect of Coriolis terms on the calculation is indistinguishable, at least at the particular buoy locations considered.

Fig. 15 summarizes the synoptic results. The center panel displays the envelope of maximum water surface elevation for the complete model. The upper panel displayed the difference of the model results with dispersion and the model results without dispersion. The presence of dispersion in the calculation leads to local changes in maximum wave height envelope of up to 20 cm even in
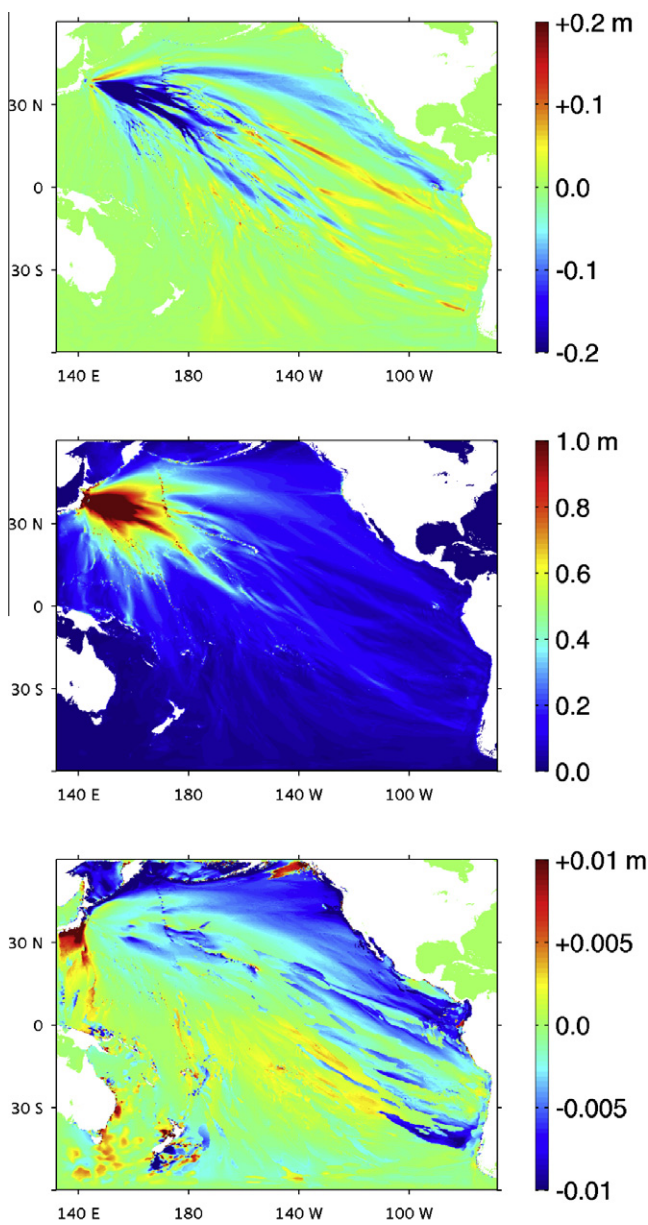

Fig. 15. Envelope of maximum computed wave elevation with FUNWAVE-TVD in spherical ($2'$) Pacific grid: difference between maximum wave height envelope with and without dispersion (upper panel); result with dispersion and Coriolis terms (center panel); and difference between maximum wave height envelope with and without Coriolis terms (lower panel).
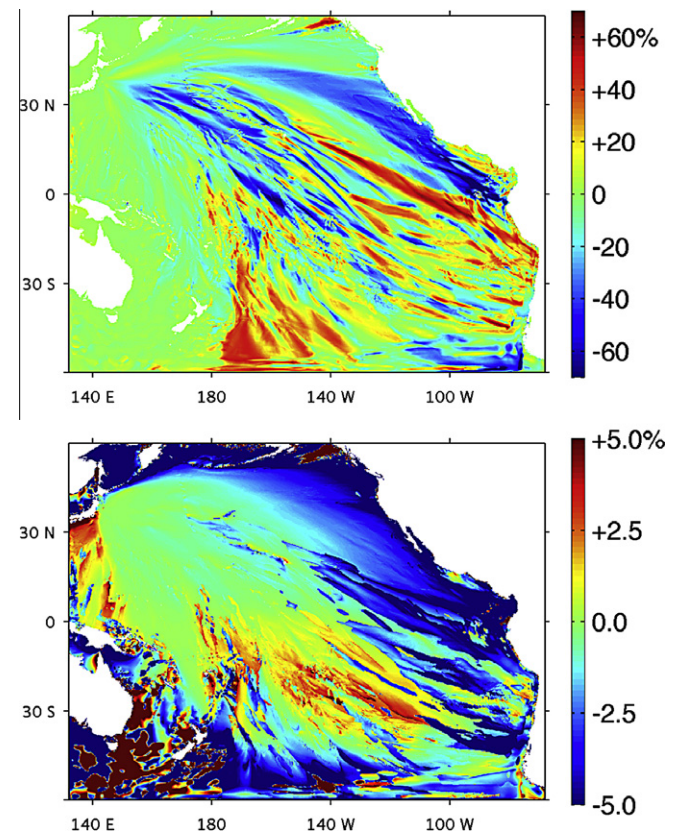

Fig. 16. Percent change in maximum wave height envelope for the Tohoku-oki tsunami for (top) simulations with and without dispersion and (bottom) simulations with and without Coriolis.

the deep ocean, which represents a significant deviation in model predictions with and without dispersion incorporated. In contrast, the lower panel in Fig. 15 indicates that the effect of Coriolis on the calculation is relatively minor, with deviations in wave amplitude on the order of a centimeter over the entire ocean basin. The presence or absence of Coriolis effects in the calculations does not lead to a practical difference in the form or amplitude of modeled waves for the Tohoku-oki simulation. Coriolis force causes waves to the right of the main direction of travel to be generally higher than they would be without it, indicating a subtle shift of the initial progressive wave pattern to the right of the rotation-free direction of propagation in the generation region, consistent with results for E–W oriented dipolar sources in the Northern hemisphere in the previous section.

Fig. 16 provides an additional view of the synoptic results, with the absolute wave height difference plots of Fig. 15 being replaced by plots of percent change resulting from taking the ratio of the difference plots to the full model simulation. The top panel indicates that dispersion has a pronounced effect on wave height distribution in the far field. There is an overall tendency for the dispersive simulation to lead to a reduction of wave height in the relative near field down wave of the source. However, this effect is partially reversed in the far field, where waves are often significantly larger in the dispersive case than the nondispersive case. This effect is partially due to a simple spatial shifting of concentrated wave energy in lateral directions, as evidenced by a pattern of positive and negative deviations along transects perpendicular to the main propagation direction. However, there is a net overall tendency towards increased wave height in the far field, indicating a systematic change in wave form due to dispersive effects.

In contrast, percent changes due to Coriolis effects are on the order of a few percent at most, and are likely to be insignificant relative to uncertainties in source configuration and other factors in a realistic simulation. Changes along the main propagation direction are on the order of ±3% in the far field. These values are consistent with previous results for simulations of the Cumbre Vieja volcano event described by Løvholt et al. (2008). The maximum effect of Coriolis is noticed along boundaries to the north and east (or to the left of the main propagation direction) where Coriolis effects reduce wave heights by up to 5%, and to the south and west (or to the right of the main propagation direction), where results are relatively increased, particularly in regions that are strongly shadowed by island chains.

5. Conclusions

We have derived fully nonlinear Boussinesq equations for weakly dispersive wave propagation on the surface of a rotating sphere, including Coriolis effects. The model equations incorporate improved dispersion following Nwogu (1993) and Løvholt et al. (2008). The weakly nonlinear version of the model is implemented using a Godunov-type method with a fourth-order MUSCL-TVD scheme in time and a third-order SSP Runge–Kutta scheme. The model is implemented using a domain decomposition technique and optimized for parallel computer clusters using MPI. Model speedup tests with multiple processors show a nearly linear speed-up, suggesting that such a Boussinesq model can be efficiently used for modeling global wave propagation.

A scaling analysis indicates that the importance of frequency dispersion should increase with a decrease in tsunami source width, and that effects of Coriolis force should increase with an increase of the source width. The importance of dispersive effects both in the far field of large sources as well as in the near field of compact, SMF-like sources is established using idealized examples. In contrast, it is seen that tsunami wave trains corresponding to typical wavelengths for co-seismic events are relatively unaffected

by rotational effects, and it is unclear that their retention in the model is a necessary part of obtaining realistic simulations. These results are in line with recent suggestions of Kowalik et al. (2005) and Løvholt et al. (2008, 2012). As the Coriolis terms do not represent a difficulty in developing the numerical scheme itself, though, there is little reason to argue that they should not be retained for completeness.

A simulation of the Tohoku-oki event and comparison to far-field DART buoy observations provides a strong test of the accuracy of the seismic/GPS source developed by Grilli et al. (2012a), which appears to be the most accurate available co-seismic source among those which are developed without input from hydrodynamic data. (For contrast, see the recent work of Løvholt et al. (2012), where the inclusion of hydrodynamic measurements is probably the strongest factor guiding the choice of source configuration.) Grilli et al. (2012b) have recently hypothesized that an additional SMF component of the event is crucial to an overall understanding of the observed tsunami properties, both in terms of modeling coastal inundation and in reproducing short period oscillations observed in GPS and closer DART buoy records. The far field DART buoy records examined here do not provide a clear picture of these additional short wave effects, as they have either dispersed at these distances or are buried within additional under-resolved scattering effects from nearby shelf and coastal boundaries.

References

Chen, Q., 2006. Fully nonlinear Boussinesq-type equations for waves and currents over porous beds. J. Eng. Mech. 132, 220–230.

Chen, Q., Kirby, J.T., Dalrymple, R.A., Kennedy, A.B., Chawla, A., 2000. Boussinesq modeling of wave transformation, breaking and runup. II: two horizontal dimensions. J. Waterway, Port, Coastal Ocean Eng. 126, 48–56.

Erduran, K.S., Ilic, S., Kutija, V., 2005. Hybrid finite-volume finite-difference scheme for the solution of Boussinesq equations. Int. J. Numer. Methods Fluids 49, 1213–1232.

Glimsdal, S., Pedersen, G., Atakan, K., Harbitz, C.B., Langtangen, H., Løvholt, F., 2006. Propagation of the December 26, 2004 Indian Ocean tsunami: effects of dispersion and source characteristics. Int. J. Fluid Mech. Res. 33 (1), 15–43.

Gottlieb, S., Shu, G.-W., Tadmor, T., 2001. Strong stability-preserving high-order time discretization methods. SIAM Rev. 43 (1), 89–112.

Grilli, S.T., Ioualalen, M., Asavanant, J., Shi, F., Kirby, J.T., Watts, P., 2007. Source constraints and model simulation of the December 26, 2004 Indian Ocean tsunami. J. Waterway, Port, Coastal Ocean Eng. 133, 414–428.

Grilli, S.T., Harris, J.C., Tajalli Bakhsh, T., Masterlark, T.L., Kyriakopoulos, C., Kirby, J.T., Shi, F., 2012a. Numerical simulation of the 2011 Tohoku tsunami based on a new transient FEM co-seismic source: comparison to far- and near-field observations. Pure Appl. Geophys.. http://dx.doi.org/10.1007/s00024-012-0528-y.

Grilli, S.T., Harris, J.C., Tappin, D.R., Masterlark, T., Kirby, J.T., Shi, F., Ma, G., 2012b. A multisource origin for the Tohoku-oki 2011 tsunami earthquake and seabed failure. Nature Comm., submitted for publication.

Grue, J., Pelinovsky, E.N., Fructus, D., Talipova, T., Kharif, C., 2008. Formation of undular bores and solitary waves in the Strait of Malacca caused by the 26 December 2004 Indian Ocean tsunami. J. Geophys. Res. 113, C05008. http://dx.doi.org/10.1029/2007JC004343.

Horillo, J., Kowalik, Z., Shigihara, Y., 2006. Wave dispersion study in the Indian Ocean-tsunami of December 26, 2004. Marine Geodesy 29, 149–166.

Ioualalen, M., Asavanant, J., Kaewbanjak, N., Grilli, S.T., Kirby, J.T., Watts, P., 2007. Modeling the 26th December 2004 Indian Ocean tsunami: case study of impact in Thailand. J. Geophys. Res. 112, C07024. http://dx.doi.org/10.1029/2006JC003850.

Kajiura, K., 1963. The leading wave of a tsunami. Bull. Earthquake Res. Inst. 41, 535–571.

Kennedy, A.B., Chen, Q., Kirby, J.T., Dalrymple, R.A., 2000. Boussinesq modeling of wave transformation, breaking and runup. I: one dimension. J. Waterway, Port, Coastal Ocean Eng. 126, 39–47.

Kennedy, A.B., Kirby, J.T., Chen, Q., Dalrymple, R.A., 2001. Boussinesq-type equations with improved nonlinear performance. Wave Motion 33, 225–243.

Kowalik, Z., Knight, W., Logan, T., Whitmore, P., 2005. Numerical modeling of the global tsunami: Indonesian tsunami of 26 December 2004. Sci. Tsunami Haz. 23, 40–56.

Kulikov, E., 2005. Dispersion of the Sumatra tsunami waves in the Indian Ocean detected by satellite altimetry. Rep. from P.P. Shirshov Institute of Oceanology, Russian Academy of Sciences, Moscow

Løvholt, F., Pedersen, G., Gisler, G., 2008. Oceanic propagation of a potential tsunami from the La Palma Island. J. Geophys. Res. 113, C09026. http://dx.doi.org/10.1029/2007JC004603.

Løvholt, F., Kaiser, G., Glimsdal, S., Scheele, L., Harbitz, C.B., Pedersen, G., 2012. Modeling propagation and inundation of the 11 March 2011 Tohoku tsunami. Nat. Haz. Earth Syst. Sci. 12, 1017–1028.

Ma, G., Shi, F., Kirby, J.T., 2012. Shock-capturing non-hydrostatic model for fully dispersive surface wave processes. Ocean Modell. 43–44, 22–35.

Masterlark, T., 2003. Finite element model predictions of static deformation from dislocation sources in a subduction zone: sensitivities to homogeneous, isotropic, Poisson-solid, and half-space assumptions. J. Geophys. Res. 108 (B11). http://dx.doi.org/10.1029/ 2002JB002296, 17pp.

Naik, N.H., Naik, V.K., Nicoules, M., 1993. Parallelization of a class of implicit finite difference schemes in computational fluid dynamics. Int. J. High Speed Comput. 5, 1–50.

Nwogu, O., 1993. Alternative form of the Boussinesq equations for nearshore wave propagation. J. Waterway, Port, Coastal Ocean Eng. 119, 618–638.

Pedlosky, J., 1979. Geophysical Fluid Dynamics. Springer-Verlag, New York, 624pp.

Pophet, N., Kaewbanjak, N., Asavanant, J., Ioualalen, M., 2011. High grid resolution and parallelized tsunami simulation with fully nonlinear Boussinesq equations. Comput. Fluids 40, 258–268.

Roeber, V., Cheung, K.F., Kobayashi, M.H., 2010. Shock-capturing Boussinesq-type model for nearshore wave processes. Coastal Eng. 57, 407–423.

Shi, F., Dalrymple, R.A., Kirby, J.T., Chen, Q., Kennedy, A.B., 2001. A fully nonlinear Boussinesq model in generalized curvilinear coordinates. Coastal Eng. 42, 337–358.

Shi, F., Kirby, J.T., Harris, J.C., Geiman, J.D., Grilli, S.T., 2012a. A high-order adaptive time-stepping TVD solver for Boussinesq modeling of breaking waves and coastal inundation. Ocean Modell. 43–44, 36–51.

Shi, F., Kirby, J.T., Tehranirad, B., 2012b. Tsunami benchmark results for spherical coordinate version of FUNWAVE-TVD (Version 1.1). Research Report No. CACR-12-02, Center for Applied Coastal Research, University of Delaware, Newark.

Shiach, J.B., Mingham, C.G., 2009. A temporally second-order accurate Godunov-type scheme for solving the extended Boussinesq equations. Coastal Eng. 56, 32–45.

Shuto, N., 1985. The Nihonkai-Chubu earthquake tsunami on the north Akita Coast. Coastal Eng. Jpn. 28, 255–264.

Shuto, N., Goto, C., Imamura, F., 1990. Numerical simulation as a means of warning for near field tsunamis. Coastal Eng. Jpn. 33, 173–193.

Sitanggang, K., Lynett, P., 2005. Parallel computation of a highly nonlinear Boussinesq equation model through domain decomposition. Int. J. Numer. Methods Fluids 49, 57–74.

Son, S., Lynett, P.J., Kim, D.-H., 2011. Nested and multi-physics modeling of tsunami evolution from generation to inundation. Ocean Modell. 38, 96–113.

Synolakis, C.E., Bernard, E.N., Titov, V.V., Kanoglu, U., González, F.I., 2007. Standards, criteria, and procedures for NOAA evaluation of tsunami numerical models. NOAA Tech, Memo. OAR PMEL-135, Pacific Mar. Env. Lab., Seattle.

Tappin, D.R., Watts, P., Grilli, S.T., 2008. The Papua New Guinea tsunami of 1998: anatomy of a catastrophic event. Nat. Haz. Earth Syst. Sci. 8, 243–266.

Tonelli, M., Petti, M., 2009. Hybrid finite volume–finite difference scheme for 2DH improved Boussinesq equations. Coastal Eng. 56, 609–620.

Wei, G., Kirby, J.T., Grilli, S.T., Subramanya, R., 1995. A fully nonlinear Boussinesq model for surface waves. I. Highly nonlinear, unsteady waves. J. Fluid Mech. 294, 71–92.

Yamamoto, S., Daiguji, H., 1993. Higher-order-accurate upwind schemes for solving the compressible Euler and Navier–Stokes equations. Comput. Fluids 22, 259–270.

Yamazaki, Y., Cheung, K.F., Kowalik, Z., 2011. Depth-integrated, non-hydrostatic model with grid nesting for tsunami generation, propagation, and run-up. Int. J. Numer. Methods Fluids 67, 2081–2107.

Yoon, S.B., 2002. Propagation of distant tsunamis over slowly varying topography. J. Geophys. Res. 107, C10. http://dx.doi.org/10.1029/2001JC000791, 3140.

Zhou, H., Moore, C.W., Wei, Y., Titov, V.V., 2011. A nested-grid Boussinesq-type approach to modelling dispersive propagation and runup of landslide-generated tsunamis. Nat. Haz. Earth Syst. Sci. 11, 2677–2697.